Politecnico di Torino

RWTH AACHEN UNIVERSITY

Modeling and Simulation of an Oxygen Exchange Induced Resistive Switching in a Two Layer Valence Change Memory Cell

Master Thesis

M.Sc. in Nanotechnologies for ICTs

Author:
Aria Sharifian
s289756

Supervisors:
Rainer Waser
Carlo Ricciardi

Abstract

Some performances of the resistive switching mechanisms in Redox-based Random Access Memory (ReRAM) Valence Change Mechanism (VCM) devices are listed to make it one of the candidates for the future innovation of non-volatile memory application. There is a need for detailed and precise explanations of their microscopic and nanoscopic behaviors.

Hence, in this thesis, features of the complex dynamics of bipolar resistive switching of ReRAM devices, more specifically VCM resistive memory devices with HfOx/TaOx bilayer stacks, are brought to light. A series of one-dimensional simulations with the finite element method is carried out using COMSOL Multiphysics software to investigate the impact of applied external biases on internal properties such as oxygen vacancy concentration and conduction band energies. These are done by two different approaches direct implementation differential equations and using built-in physical models from COMSOL Multiphysics software.

From the results, it can be seen that there is a great change in the internal properties of the device with the application of the pulsed voltages, and the changes depend on the magnitude, polarity, and duration of the applied bias. In other words, the effects of magnification of the device's conductivity on voltages and duration, respectively, bring distinct resistance states to the device which may be either a high resistance state or a low resistance state. More specifically, this can be seen through the characteristics of the plotted device resistance versus the oxygen vacancy concentration. It is possible to observe that the increase in oxygen vacancy concentration in the conducting oxide layer is always accompanied by an increase in device resistance.

In this work it is tried to reproduce these findings using the Semiconductor Module of COMSOL Multiphysics. Yet, there are certain problems in modeling the ions as charge carriers and the phenomenon of direct tunneling. In order to prevent these problems, the possibility of enhancing the methodology of simulation through the development of new advanced physical models and modules is worked out.

It goes on to examine the effect of different electrode materials on device behavior in such a manner that symmetric compositions of electrodes would cause symmetrical oxygen vacancy distributions within the device. The material selection and their corresponding dependence on electrode metal work functions further underscores the importance of material selection in device design.

Overall, this thesis sheds light on the complicated nature of VCM ReRAM devices, in the context

of simulation techniques and research in general, in order to exploit their potential to the hilt with rising memory technologies.

Acknowledgments

I would like to express my gratitude to everyone at RWTH-Aachen University's IWE-2 Institute who supported me during my thesis. Special thanks to Professor Rainer Waser, Dr. Stephan Menzel for letting me join their team, and my daily supervisor Nils Sommer for his invaluable guidance and support.

I also want to acknowledge the contributions of former students Astrid Marchewka and Fenja Berg, whose work on the implementing models greatly benefited my research.

To my professors and friends at Politecnico di Torino, thank you for your support throughout my master's studies, specially Professor Carlo Ricciardi who helped me to find this great opportunity to conduct my thesis abroad.

And finally, heartfelt thanks to my family for their unwavering support throughout my academic journey.

Aria Sharifian - May, 2024 Aachen

Table of Contents

Chapter 1

Introduction

Non-Volatile Memory (NVM) stands as a prevalent category of computer memories, capable of preserving stored data even in the absence of power. High-density of cells, low fabrication costs, fast read and write speeds, low energy consumption, and high write cyclability (i.e. high performance and endurance) are among the desired characteristics of NVMs. Nowadays Silicon-based flash memory devices are the most used NVM due to their high density and economical advantages. Nevertheless, they face challenges such as limited endurance, low write speeds, and the requirement of high voltages for writing operations [1].

Memristors (memory-resistor) or memristive devices can fulfill these requirements. They are highly scale-able, fast in writing operations and low energy consuming in switching mechanisms. Two-terminal memristor devices can retain their internal resistance state according to previously applied voltages or currents. They are special in a sense that their behavior cannot be replicated using conventional electronic circuit elements [2].

Memristors were initially predicted as the fourth passive electrical circuit element, which can relate the electric charge with the magnetic flux [3]. A better description of memristors is devices with pinched-hysteresis loop in voltage-current characteristics, the loop size is frequency dependant. The natural application for these kind of devices is Resistive Random Access Memory (RRAM), although other applications for example in alternative logic architectures can be considered for them [4].

The main idea behind redox-based random access memories (ReRAMs), is the fact that they can be switched between two resistance states, i.e., High Resistance State (HRS or OFF) or Low Resistance State (LRS or ON). Based on the state of the ReRAM memory cell, a bit of information is stored through changes in the the dielectric material situated between the two metal electrodes [5]. As it can be seen in the Figure 1.1, based on the resistive switching mechanisms, ReRAMs can be classified.

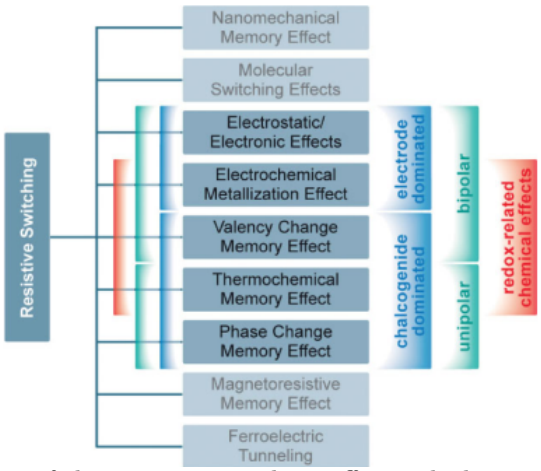

Figure 1.1: Classification of the resistive switching effects which are considered for non-volatile memory applications. From: [1], license number: 5787050663774.

Switching between a crystalline phase (ON-state) and an amorphous phase (OFF-state) is used in phase change memories (PCM) [6]. In electro-chemical metallization (ECM), an electro-chemical deposition and dissolution of a certain metal inside the cell is utilized to achieve resistance switching [7]. For example, Ag ions can drift inside a 'I' layer which can result in the growth of a highly conductive filament of Ag, so the On state is achieved [8]. When the polarity of the applied voltage is switched, a dissolution of the filament happens, so the cell is reset into the OFF state. Also there are thermo-chemical mechanisms (TCM) which are based on the changes in stochiometry due to temperature changes inside the material [1].

The mechanism that is in the focus of this thesis is Valence Change Memory effect. The main principle of VCM can be seen as change in the valence state of the material in a resistive layer which changes the conductivity of the cell [9]. Lately, there has been significant interest in bilayer resistive random access memories due to their suggested superior endurance and performance in comparison to single-layer devices [1].

In this thesis, we are focusing on bi-layer VCM structures in which two layers of resistive materials are used. Lately, there has been significant interest in bilayer resistive random access memories due to their suggested superior endurance and performance in comparison to single-layer devices [10]. To gain a theoretical comprehension of the physical processes which are involved in resistive switching bi-layer VCM devices, numerical simulations of these ReRAMs are becoming increasingly crucial [11]. A detailed numerical model to analyze VCM resistive switching is done by Astrid Marchewka [12]. In this thesis the model is extended such as it enables to simulate bi-layer structures and analyze their behavior.

Chapter 2

Theoretical principles

This chapter serves the purpose of introducing the theoretical foundations which are essential to this thesis. It explicates the fundamental principles underlying the used device.

2.1 General characteristics of resistive switching devices

The resistive switching phenomenon pertains to the reversible alteration of a material's resistance state under external electrical stimuli, transitioning between two or more stable states. This property is harnessed in the development of re-writable nonvolatile memory devices, commonly known as resistance (switching) random-access memories. These memories comprise numerous resistively switching memory cells arranged in a structured memory matrix [12].
Broadly, a Resistive Random Access Memory (RRAM) device is composed of a Metal-Insulator-Metal (MIM) structure, wherein the insulating or resistive layer is positioned between two conductive metal layers [1].
Typically, the resistance states in this context are designated as the High Resistance State (HRS) and Low Resistance State (LRS). The HRS is often referred to as the OFF state, while the LRS is designated as the ON state. The transition from the High Resistance State to Low Resistance State is termed "Set", whereas the transition from LRS to HRS is referred to as "Reset". These transitions can be achieved by applying either a voltage or an electric current. Frequently, an electroforming step is required in the cell before activating the switching mechanism [1].
In the context of voltage-driven resistive switching, the operational characteristics can be categorized into two types: unipolar and bipolar switching. Unipolar switching occurs independently of the applied voltage's polarity. In this mode, the Set process necessitates a higher voltage compared to the Reset process. Within the bipolar switching mode, distinct voltage polarities are requisite for the Set and Reset processes. This asymmetry in voltage response arises due to a certain degree of asymmetry in the device. The operational dynamics of these modes are illustrated schematically in Figure 2.1.

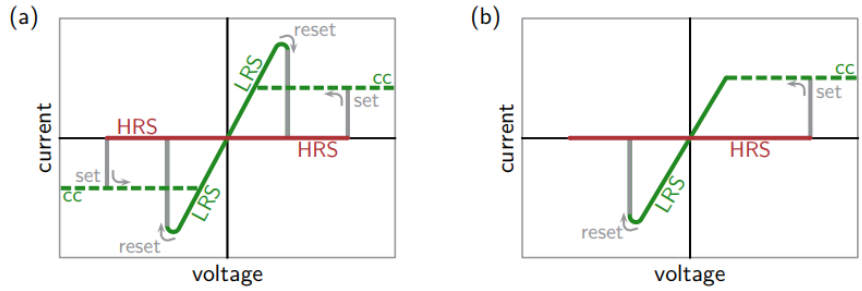

Figure 2.1: a) Illustration of unipolar switching, where both Set and Reset processes are unaffected by the voltage polarity. b) Diagram depicting bipolar switching, where the Set process occurs at one voltage polarity, and the Reset process takes place at the reverse polarity. Adapted from: [1], license number: 5787050663774.

2.2 Valence change memory

In VCM, the metal-insulator-metal structure comprises an active electrode (AE) and an Ohmic counter electrode (OE). The insulating layer is positioned between these electrodes functions as a mixed-ionic-electronic conducting layer [13].
While a detailed comprehension of the underlying processes is currently not available, there is a general consensus regarding resistive switching in VCM cells. This consensus suggests a reliance on oxygen-vacancy migration and associated redox reactions [14].
Consequently, reduction and oxidation processes precipitate valence changes within the cation sublattice, thereby justifying the naming "valence-change memory". Certain attributes of VCM structures include their bipolar switching nature and the necessity for an electroforming step to facilitate the switching process.

2.2.1 Understanding VCM phenomena in crystalline structures using $SrTiO_3$ model

Valence change mechanism can be explained using a $SrTiO_3$ model. $SrTiO_3$ belongs to the Perovskite class and features a cubic lattice structure. Within the unit cell, a titanium (Ti) atom is positioned at the center, encompassed by eight strontium (Sr) atoms situated at the corners of the cell. The four oxygen (O) atoms are strategically positioned at the face center in proximity to the titanium cations [15], as depicted schematically in Figure 2.2.
In the case of $SrTiO_3$, the electrons originate from the last s-orbital and the inner d-orbital of titanium atom participating in chemical bondings with oxygen. Consequently, titanium can release four electrons for bonding, transforming into a fourfold charged positive ion, Ti^{4+}. This release of electrons is named as oxidation. This oxidation results in a deficiency of conduction electrons available for current transport, leading to insulating behavior in the oxide. However, in the presence of oxygen vacancies within the structure of $SrTiO_3$, not all electrons from the outer shells of titanium are required for oxygen bonding. Titanium undergoes a local reduction, changing to a double or threefold charged ion, Ti^{2+} or Ti^{3+}. The liberated electrons in the conduction band contribute to the current transport, thereby reducing the resistivity of the oxide. This dynamic interplay of reduction and oxidation by oxygen induces a change in the valence state of the oxide [1].

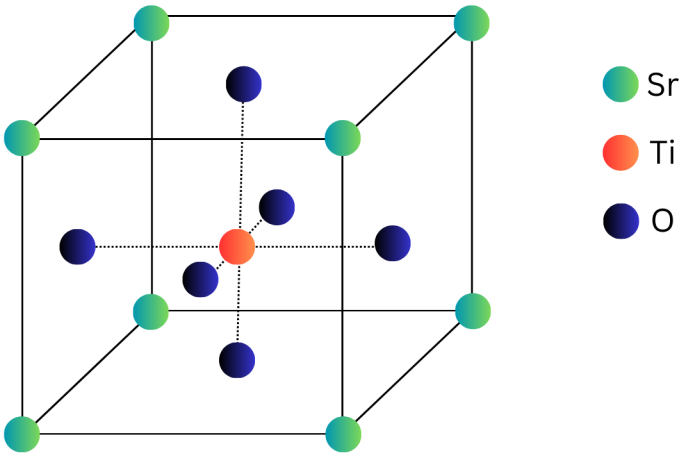

Figure 2.2: Sketch of the lattice cubic structure of $SrTiO_3$.

Oxygen vacancies in the crystal lattice constitute point defects. Generally, point defects include vacancies, interstitials, and substitutional effects. in its original state, how much the lattice is disordered depends on different equilibrium situations involving defects. The Schottky equilibrium represents one such equilibrium, describing the formation of anions and cation vacancies at elevated temperatures. Additionally, the equilibria involving oxygen exchange between the lattice and the ambient atmosphere, as well as the electronic equilibrium governing the recombination of electron-hole pairs, significantly influence the lattice disorder [13]. Further elaboration is available in [13].

2.3 Charge transport principles

This section introduces and provides a brief explanation of the electronic and ionic transportation fundamentals employed in the study of Valence Change Memory (VCM) within this thesis.

2.3.1 Schottky contacts

When a metal and a semiconductor come into contact and reach thermal equilibrium, their Fermi energy levels become equal. Achieving this equilibrium involves adjusting the semiconductor's energy level by an amount known as the barrier height, which is equal to the difference between the two work functions. The work function, denoted as qW_{M} for metals and $q\chi_{\mathrm{cs}} + q\phi_{\mathrm{n}}$ for semiconductors, represents the energy gap between the vacuum level and the Fermi energy level. Here, $q\chi_{\mathrm{cs}}$ is the electron affinity measured from the bottom of the conduction band (E_{C}) to the vacuum level, and the energy difference between E_{C} and the Fermi level is $q\phi_{\mathrm{n}}$. In these expressions, q represents the elementary positive charge. Therefore, the barrier height can be expressed as [16]:

$$q\phi_{\mathrm{Bn0}} = q(W_{\mathrm{M}} - \chi_{\mathrm{sc}}) \tag{2.1}$$

A graphical representation (band diagram) of a Schottky barrier formed between a metal and a semiconductor is depicted in Figure 2.3.

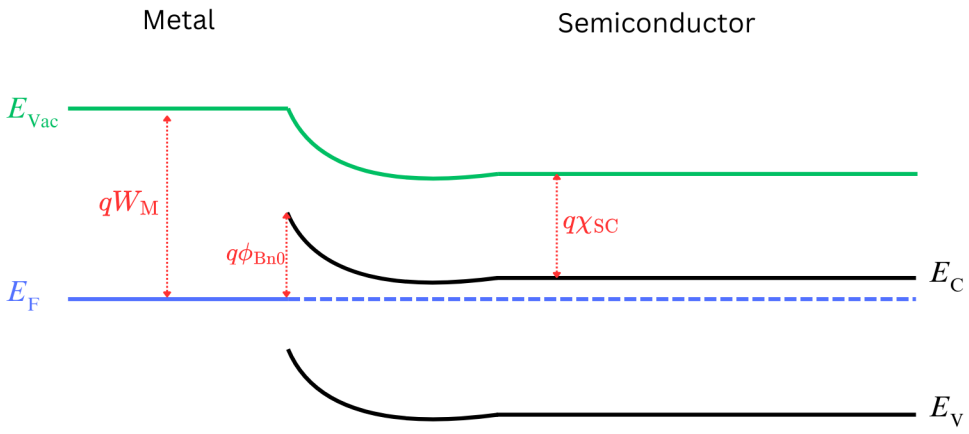

Figure 2.3: Energy-band diagram of a metal/n-type semiconductor contact.

Nevertheless, the accuracy of the Equation 2.1 is not always upheld in experiments. Real-world scenarios often involve a physical separation between the two materials, potential presence of interface states, and the possibility of image-force lowering affecting the barrier [16].

2.3.2 Ionic transport

Given that the switching behavior of Valence Change Memory devices is determined by oxygen vacancies, understanding their transport characteristics is crucial. The ion transport mechanisms relevant to VCM devices contains thermo-diffusion, drift, and diffusion. In essence, ion transport relies on hopping within an energy landscape, therefore, overcoming an activation energy (W_{A}) is necessary. In the absence of an external field, the ion hopping is due to isotropic diffusion movement. Conversely, the presence of an external electrical field (E) arising from an applied voltage (V) induces a reduction in the energy barrier along the field direction by $-e \cdot a \cdot \frac{E}{2}$, where e represents the electron charge and a is the hopping distance. This field-induced modification facilitates ion movement in the direction of the field, leading to a drift motion. A sketch of the ionic transport in presences and the absence of the external force is depicted in Figure 2.4.

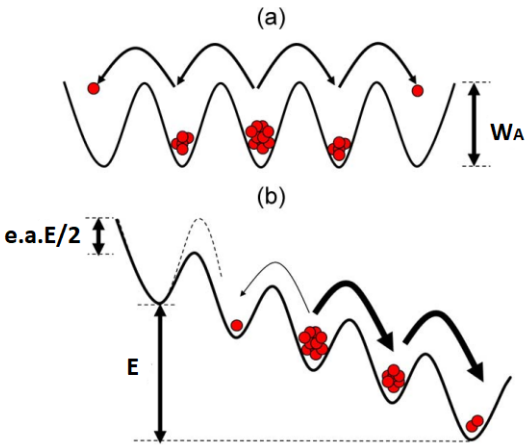

Figure 2.4: Schematic of the potential energy landscape for ion hopping at a) absence of external force b) when applying voltage . Redrawn form [17] © 2012 IEEE.

The comprehensive ion migration is understood through the superposition of all transport modes. In the context of Valence Change Memory devices, this implies that the migration of oxygen vacancies within the crystal lattice results in a localized alteration of the oxide stoichiometry. Regions enriched with oxygen vacancies consequently exhibit an increased availability of conduction electrons for electronic transport [17].

2.3.3 Tunneling mechanism

In classical physics, the transmission or reflection of electrons when encountering an energy barrier is determined by the energy of the electron and the energy level of the barrier. If the electron possesses greater energy, it will be transmitted, while lower energy results in reflection. Quantum mechanics introduces the phenomenon of tunneling, wherein electrons may traverse a barrier with energy lower than the barrier itself [11]. The extent of tunneling is influenced by various factors. Figure 2.5 illustrates two examples comparing classical mechanics and quantum mechanics for tunneling through a barrier.

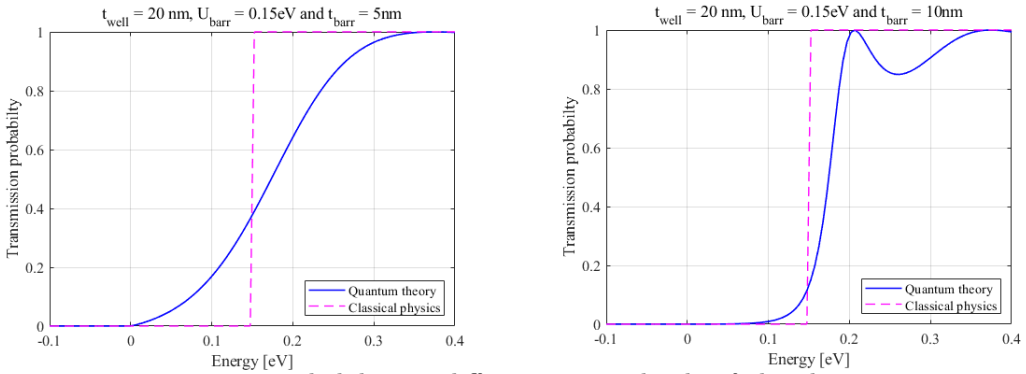

Figure 2.5: Transmission probability in different energy levels of the electrons in an energy barrier based on the classical and quantum mechanics equations. On left and on the right the amount of the transmission is different. This is due to the fact that thickness of the barrier is changed.

A mathematical model for the tunneling process at the interface of the connection between two different materials is provided by Tsu and Esaki [18]. In this model, the tunneling through the barrier

is expressed as:

$$J_{\text{tunnel}} = \frac{4\pi m_{\text{eff}} q}{h^3} \int_{E_{\text{c,min}}}^{E_{\text{c,max}}} TC(E_{\text{z}}) N_{\text{sup}}(E_{\text{z}}) \mathrm{d}E_{\text{z}} \tag{2.2}$$

In the provided expression, h represents Planck's constant, m_{eff} denotes the effective mass of the particle, and q stands for the elementary charge. The transmission coefficient (TC), corresponding to the transmission probability, is determined by the electron's energy levels (E_{z}), and N_{sup} represents the supply function for that specific energy level. The terms $E_{\text{c,min}}$ and $E_{\text{c,max}}$ denote the minimum and maximum values of the energy barrier at the interface. Detailed equations for the transmission coefficient and supply function are elaborated in Chapter 3.

2.3.4 Thermo-ionic emission

At different temperatures, electrons may occupy higher energy levels. Thermally excited electrons can possess energy greater than the potential barrier they encounter, leading to a conduction mechanism across the potential barrier known as thermionic emission. The distinction between thermionic emission and the tunneling process lies in the fact that in thermionic emission only the height (energy) of the barrier is significant, not its shape [16]. The current density for thermionic emission can be calculated similarly to tunneling current density. The key difference is that thermally induced electrons have higher energy than the barrier, resulting in a transmission probability equal to 1. Therefore, thermionic emission transport can be expressed as:

$$J_{\text{thermo-ionic}} = \frac{4\pi m_{\text{eff}} q}{h^3} \int_{E_{\text{c,min}}}^{E_{\text{c,max}}} N_{\text{sup}}(E_{\text{z}}) \mathrm{d}E_{\text{z}} \tag{2.3}$$

2.4 ReRAM characteristics

In this section, key attributes and properties essential for comprehending resistive switching in VCM ReRAMs are briefly introduced and clarified.

2.4.1 Electro-forming of filament

Prior to any resistance switching in the Valence Change Memory device, an essential electroforming step is required. The electroforming step involves applying a voltage to induce a local reduction of the oxide, leading to the generation of oxygen vacancies. This process results in the creation of doubly ionized oxygen vacancies that migrate toward the electrode [19]. As a consequence, a conductive filament is formed inside the oxide layer, as illustrated in Figure 2.6.

Following the formation of the conductive filament, the Valence Change Memory device can be set to either a High Resistance State or a Low Resistance State depending on the polarity of the applied voltage and the characteristics of the oxide material. Typically, filament growth initiates from the ohmic electrode, characterized by a lower potential barrier, and progresses towards the active electrode. Titanium is commonly employed as the material for the ohmic electrode, while gold or platinum is frequently used for the active electrode.

The forming voltage, which denotes the voltage which is required for the electroforming process, is greater than the Set voltage and is depending on the thickness of the oxide (middle layer). During the forming process, characterized by elevated voltages and currents, the localized temperatures are expected to be very high [13].

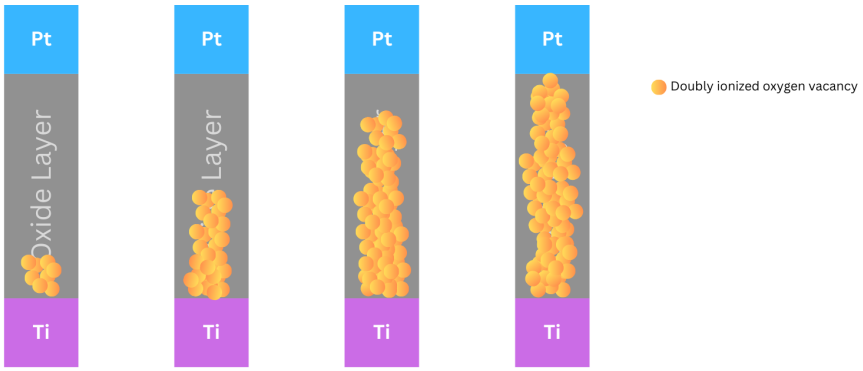

Figure 2.6: By applying the forming voltage, a filament of oxygen vacancies is built starting from the Ohomic electrode.

2.4.2 SET and RESET in VCM

The stable switching process in VCM devices transpires in the region between the plug and the active electrode, with the plug representing the segment of the oxygen vacancy filament present in the OFF state. The Set process involves applying a negative voltage to the active electrode, causing the migration of oxygen vacancies toward the active electrode and a consequent reduction in the potential barrier. As a result, the cell achieves higher conductivity, entering the ON (LRS) state. Reset, on the other hand, is accomplished by applying a reversed-polarity voltage, causing oxygen vacancies to move back into the filament (plug) and leading to re-oxidation. This action returns the cell to the OFF (High Resistance State, HRS) state, characterized by low conductivity. A detailed depiction of the Set and Reset processes for a bipolar switching VCM is presented in Figure 2.7 [13].

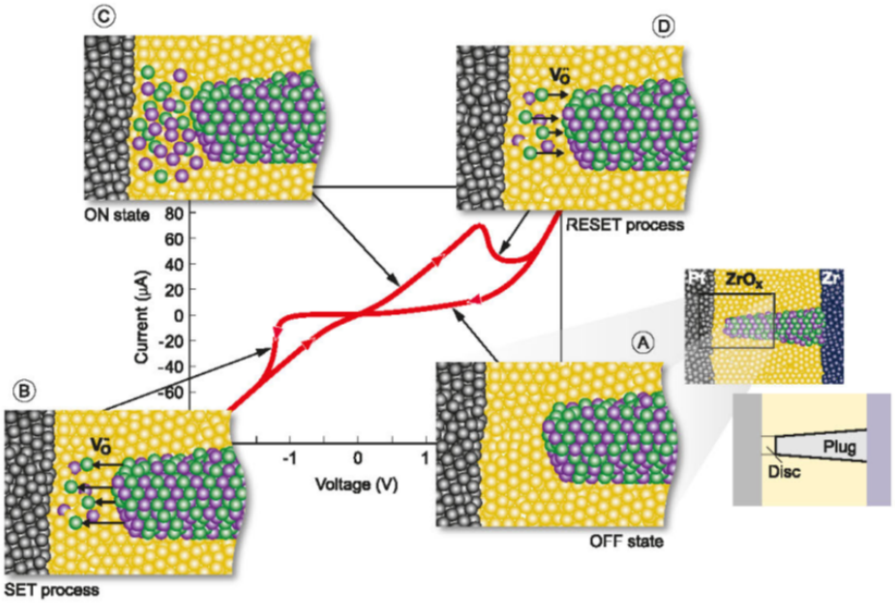

Figure 2.7: The schematic representation illustrates the Set and Reset characteristics of a Valence Change Memory (VCM) device. In the OFF state (A), there is no conducting filament between the electrodes. Upon applying a negative voltage, ions are attracted to the top electrode, resulting in the creation of a filament during the Set process (B) and leading to the ON state (C) with a conducting filament between both electrodes. Conversely, applying a positive voltage to the active electrode during the Reset process (D) prompts the migration of oxygen ions back into the plug, resulting in a measurable reset. The device then returns to the OFF state (A). This depiction is derived from [13] (https://marketplace.copyright.com/rs-ui-web/mp/license/4df5fdc4-11c2-46d8-a901-d8de4401c120/1bc1ebd0-c59a-4b64-a722-a258b16fb766).

2.4.3 Complementary switching

Beside the bipolar switching, another common type of switching is called complementary switching mechanism. The concept of the complementary switching is based on creating depletion areas near top or bottom electrode. Hence, for each voltage polarity, a depletion layer is created between the filament and one of the electrodes. In result, both ON and OFF state can be seen in positive and negative applied voltages. An example of the complementary switching is displayed in Figure 2.8
In complementary switching, the initial state is OFF, in which a gap between the bottom electrode and filament is present. By applying a positive voltage this gap is filled due to the migration of the oxygen vacancies, hence, the cell will be in ON state (Set1). By increasing the voltage further, a re-oxidation happens in near the top electrode, so the depletion gap is created between that and the filament, this will turn the cell into OFF state (Reset1). By switching the polarity and applying a negative voltage the gap near the top electrode can be closed and the cell will get to ON state again (Set2). by increasing the value of the negative voltage, a gap is created near the bottom electrode which put the cell once more in OFF state (Reset2) [20].

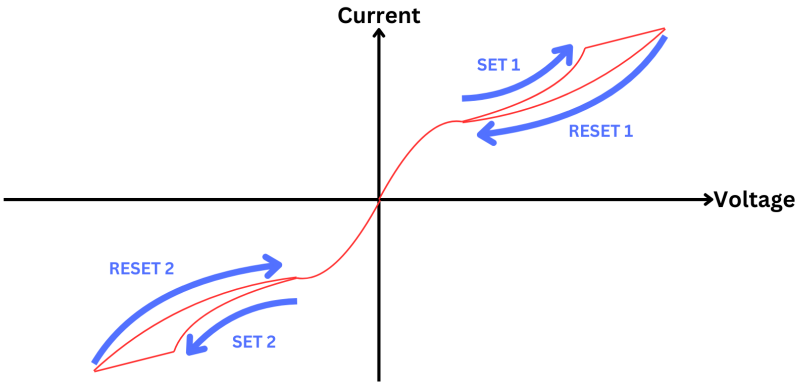

Figure 2.8: Sketch of complementary switching. In both voltage polarities HRS and LRS are present. Applying a positive voltage results in Set 1 then Reset 1. Applying negative voltage leads to Set 2 followed by Reset 2.

2.4.4 Bi-layer ReRAM

The bi-layer concept represents an innovative approach in Redox-based Random Access Memory (ReRAM) devices, involving the usage of two oxide layers between the electrodes. One possible configuration is the usage of homogeneous layers, where an oxygen-deficient layer is positioned at the Ohmic electrode, and a stoichiometric layer is placed at the active electrode, as an example: TiO2/TiO(x < 2). Another approach involves the usage of different oxide types with distinct band gap energies and formation energies, resulting in a heterogeneous bi-layer structure. An example of such a combination is Al_2O_3/TiO_2 [13].
Bi-layer Resistive Random Access Memories (RRAMs) exhibit promising attributes in terms of resistive switching behavior, demonstrating features essential for ReRAM applications. The incorporation of two oxide layers between electrodes creates advantageous characteristics to bi-layer ReRAMs, including robust endurance, accelerated switching speed, and prolonged data retention capabilities [21]. Integrating a bi-layer structure into ReRAMs not only enhances resistive switching behavior but also plays an important role in improving the device's retention and stability during prolonged use. The utilization of two oxide layers between electrodes contributes to the overall robustness of the ReRAM, ensuring sustained performance over extended periods [22].
The ReRAM investigated in this thesis features a heterogeneous bi-layer structure with a TaO_x/HfO_x interface.

2.5 Materials

In this section the two oxides which are used in the stacked VCM cell under study are introduced and briefly reviewed.

2.5.1 Hafnium oxide - HfO_x

ReRAMs utilizing HfO_2 have been extensively investigated. This is primarily because of its common application in transistor gate stacks and its notable resistive switching properties. The discussions

encompass modifications to the Schottky barrier at electrodes, the migration of electrode ions, space-charge-limited current, and the phenomenon of filamentation caused by oxygen deficiency [23].
Within the Valence Change Mechanism, materials like HfO_x have demonstrated the generation of oxygen vacancies induced by dielectric effects. in the presence of an oxygen vacancy filament, the LRS is established when the oxygen-deficient path connects to the metal electrode. Conversely, the HRS occurs when the filament is disrupted due to the re-migration of oxygen ions back to the vacancies.
Despite extensive studies on ReRAMs based on HfO_x, the precise role of oxygen vacancies in electron transport remains unclear [23].

2.5.2 Tantalum oxide - TaO_x

Until now, resistance switches based on amorphous TaO_x have been widely discussed, demonstrating notable attributes such as high switching speed, long endurance, and low operation bias voltage when compared to ReRAM devices utilizing alternative materials [24].
The switching mechanism in resistance switches relying on oxygen-deficient materials like TaO_x is commonly attributed to the drift-diffusion of oxygen ions or vacancies in the presence of an electric field.
Recent experimental investigations into the filament components in TaO_x-based resistance switches have revealed the presence of significant continuous Ta-rich regions, denoted as TaO_{1-x}, within the LRS. These Ta-rich regions play a crucial role as the conduction path in ReRAM cells. However, the origin of the switching mechanism in TaO_x-based resistance switches remains a topic of controversy. There is a strong need to elucidate the switching processes, particularly focusing on understanding the detailed structure and electronic behavior of the oxygen-deficient filament [24].

Chapter 3

Physical model for the simulation

The primary simulation model employed in this thesis is derived from the physical model outlined by Astrid Marchewka [12]. To investigate the VCM ReRAM cell with stacked layers, a 1-Dimensional model, as illustrated in Figure 3.1, is simulated using Finite Element Method (FEM) modeling within the COMSOL Multiphysics software [25].

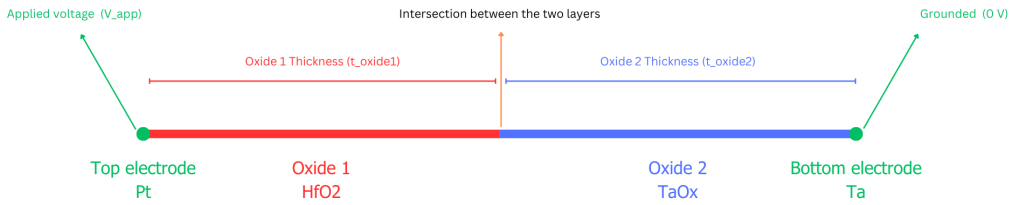

Figure 3.1: Schematic of 1D model used in simulation of bi-layer VCM cell

The simulation involves the numerical solution of four simultaneous differential equations:

- Poisson equation
- Electron continuity equation
- Ion continuity equation
- Heat conduction equation

These four equations and their boundary and initial conditions are described in this chapter.

3.1 Poisson equation

3.1.1 General model equation

The Poisson equation is solved within the both oxide regions, it is as:

$$\nabla \left(-\epsilon_0 \epsilon_\mathrm{r} \nabla \phi\right) = \rho q. \tag{3.1}$$

Here, the dependent variable is the electrostatic potential ϕ. ϵ_0 represents the free space permittivity, and ϵ_r is the relative permittivity, which is material-dependent. q denotes the elementary charge, and ρ signifies the charge density. Since donor dopants have dominant presence, the charge density considers them and the electron concentration (n), leading to:

$$\rho = -n + N_\mathrm{D}. \tag{3.2}$$

In this context, N_D represents the donor dopants concentration, with n indicating the electron density. For the studied VCM cell, only doubly ionized oxygen vacancies are considered as donors, resulting in:

$$N_\mathrm{D} = 2V_{\ddot{\mathrm{O}}}. \tag{3.3}$$

Here, $V_{\ddot{\mathrm{O}}}$ represents the oxygen vacancy concentration, determined by solving the ion continuity equation introduced in Section 3.3. The electron density (n) can be obtained using:

$$n = N_\mathrm{C} \frac{2}{\sqrt{\pi}} F_{0.5} \left(\frac{E_\mathrm{fn} - E_\mathrm{c}}{k_\mathrm{B} T} \right). \tag{3.4}$$

where k_B is the Boltzmann constant, T is the temperature (obtained using the heat conduction equation in Section 3.4), and N_C is the effective density of conduction band states, given by:

$$N_\mathrm{C} = 2 \left(\frac{2\pi m_\mathrm{eff} k_\mathrm{B} T}{h^2} \right)^{\frac{3}{2}}. \tag{3.5}$$

Here, m_eff is the electron effective density, and h represents Planck's constant.
In Equation 3.4, $F_{0.5}$ denotes the Fermi-Dirac integral of the order of $\frac{1}{2}$, E_fn is the electrons quasi-Fermi level (found by solving the electron continuity equation in the Section 3.2), and E_C is the conduction band edge energy, calculated as:

$$E_C = -\chi - q\phi. \tag{3.6}$$

where χ denotes the electron affinity. The Fermi-Dirac integral of the order of $\frac{1}{2}$ is defined as:

$$F_{0.5}(x) = \frac{1}{\Gamma(0.5+1)} \int_0^\infty \frac{t^{0.5}}{\exp(t-x)+1} \mathrm{d}t. \tag{3.7}$$

Here, Γ is the gamma function, and for this case, $x = \frac{E_\mathrm{fn} - E_\mathrm{C}}{k_\mathrm{B} T}$ and $t = \frac{E - E_\mathrm{C}}{k_\mathrm{B} T}$.

3.1.2 Boundary conditions

To establish the boundary conditions for the Poisson equation, it is essential to determine the electric potential (ϕ) at the interfaces of both the top and bottom electrodes with the oxide layers. In our

model, there exist two Schottky contacts: one at the interface of the top electrode and oxide 1, and another at the interface between oxide 2 and the bottom electrode. The general equation describing the Schottky contact potential is given by:

$$\phi_{\text{Schottky}} = -[\phi_{\text{Bn0}} + \frac{k_{\text{B}}T}{q}\text{inv}FD_{0.5}(\frac{N_{\text{D}}}{N_{\text{C}}})]. \tag{3.8}$$

Here, $\text{inv}FD_{0.5}$ is defined as the inverse Fermi-Dirac integral multiplied by $\frac{\sqrt{\pi}}{2}$, and ϕ_{Bn0} denotes the total barrier height at the interfaces, obtainable from Equation 2.1. The term $\frac{k_{\text{B}}T}{q}.\text{inv}FD_{0.5}(\frac{N_{\text{D}}}{N_{\text{C}}})$ represents the disparity between the quasi-Fermi level and the conduction band energy. An illustrative example of the Schottky contact band diagram is presented in Figure 3.2.

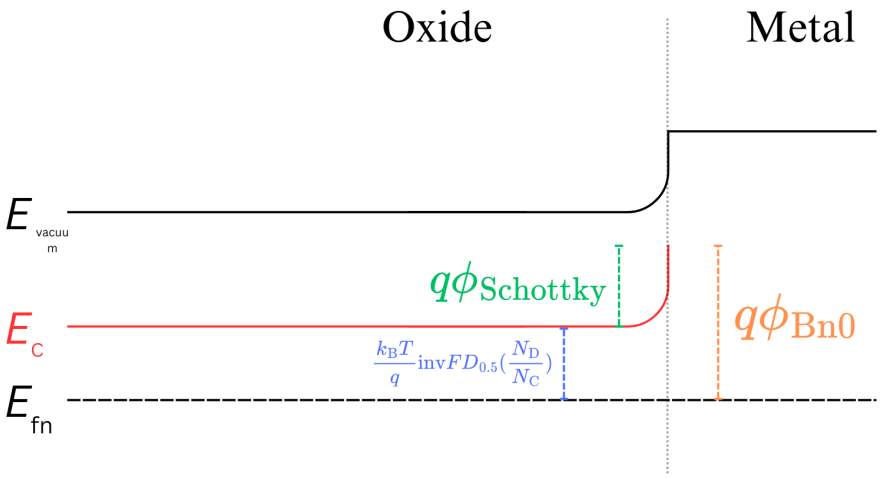

Figure 3.2: Band diagram at a Schottky contact, the Schottky potential of the interface is the green dotted line.

Due to variations in donor concentration within the oxide region, a discrepancy may arise between the intrinsic Fermi level and quasi-Fermi level. At each metal-semiconductor interface, this difference can be expressed as:

$$\phi_{\text{diff}} = \frac{E_{\text{g}}}{q \cdot 2} + \frac{k_{rmB}T}{q}\text{inv}FD_{0.5}\left(\frac{N_{\text{D}}}{N_{\text{C}}}\right). \tag{3.9}$$

Here, E_{g} denotes the band gap energy of the oxide, representing the energy gap between the valence and conduction energy bands, expressed as:

$$E_{\text{g}} = E_{\text{C}} - E_{\text{V}}. \tag{3.10}$$

Since the potentials are needed for both the top and bottom interfaces, one can determine the relative change in potentials for the top and bottom electrodes and add this to the potential of the top electrode:

$$\phi_{\text{relative}} = \phi_{\text{diff, top}} - \phi_{\text{diff, bottom}}. \tag{3.11}$$

To find this difference, consider that the quasi-Fermi levels of two semiconductors (or oxides) tend to align at their intersection. By utilizing their electron affinity, the difference in their $\frac{E_{\text{g}}}{q \cdot 2}$ can be

determined, equating to:

$$\frac{E_{\mathrm{g},1}}{2q} - \frac{E_{\mathrm{g},2}}{2q} = \frac{\chi_1 - \chi_2}{q}. \tag{3.12}$$

in which χ_1 and χ_2 are the electron affinities of the oxide 1 and oxide 2.
Similarly, the difference in $\frac{k_\mathrm{B}T}{q} \cdot \mathrm{inv}FD_{0.5}\left(\frac{N_\mathrm{D}}{N_\mathrm{C}}\right)$ can be straightforwardly calculated by:

$$\frac{k_B T_{\mathrm{top}}}{q}.\mathrm{inv}FD_{0.5}(\frac{N_{\mathrm{D,top}}}{N_{\mathrm{C,top}}}) - \frac{k_B T_{\mathrm{bottom}}}{q}.\mathrm{inv}FD_{0.5}(\frac{N_{\mathrm{D,bottom}}}{N_{\mathrm{C,bottom}}}). \tag{3.13}$$

where N_D, N_C, and T should represent the values at the interfaces. Combining Equations 3.11, 3.12, and 3.13, the relative potential difference at the top contact interface is given by:

$$\phi_{\mathrm{reletive}} = \frac{\chi_1 - \chi_2}{q} + \frac{k_\mathrm{B}T_{\mathrm{top}}}{q}.\mathrm{inv}FD_{0.5}(\frac{N_{\mathrm{D,top}}}{N_{\mathrm{C,top}}}) - \frac{k_\mathrm{B}T_{\mathrm{bottom}}}{q}.\mathrm{inv}FD_{0.5}(\frac{\mathrm{N_{D,bottom}}}{N_{\mathrm{C,bottom}}})). \tag{3.14}$$

During the simulation, we apply a voltage to the upper contact to assess the properties and functionality of Valence Change Memory. It is essential to consider this applied voltage, denoted as V_{app}, and add it to the potential of the upper electrode.
In summary, the boundary conditions for the Poisson equation are established accordingly:

$$\phi_{\mathrm{top}} = \phi_{\mathrm{Schottky-top}} + \phi_{\mathrm{relative}} + V_{\mathrm{app}}. \tag{3.15}$$

$$\phi_{\mathrm{bottom}} = \phi_{\mathrm{Schottky-bottom}}. \tag{3.16}$$

However in the implementation, of this thesis the metal work functions of the two electrode metals are directly used as the boundary condition for simplicity:

$$\phi_{\mathrm{top}} = -W_{\mathrm{M,top}} + qV_{\mathrm{app}}. \tag{3.17}$$

$$\phi_{\mathrm{bottom}} = -W_{\mathrm{M,bottom}}. \tag{3.18}$$

where $W_{\mathrm{M,top}}$ and $W_{\mathrm{M,bottom}}$ represent the metal work function of the material used as the top and bottom electrodes. In Figure 3.3, a schematic illustrating the applied boundary condition for Poisson equation is presented.

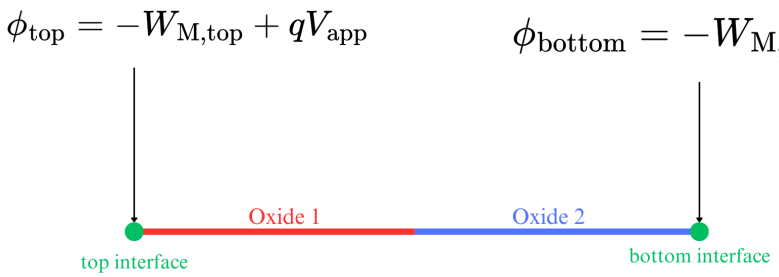

Figure 3.3: Position and value of the parameters used as boundary conditions in Poisson equation.

3.2 Electron continuity equation

3.2.1 General equation

The continuity equation for electrons is expressed in terms of the drift-diffusion equation:

$$-\frac{1}{q}\nabla j_{\text{n}} = -\frac{1}{q}\nabla(-q\mu_{\text{n}} n\nabla\phi + qD_{\text{n}}\nabla n + qnD_{\text{Tn}}\nabla T) = -R_{\text{n}}. \tag{3.19}$$

Here, μ_{n} represents the electron mobility, D_{n} is the electron diffusion coefficient, R_{n} denotes the electron recombination rate, and j_{n} is the electron current density. The term D_{Tn} stands for the thermal diffusion coefficient for electrons.
Assuming the temperature gradient is considerably smaller than the gradient of electric potential and electron density, this term can be neglected, resulting in:

$$-R_{\text{n}} = -\frac{1}{q}\nabla j_{\text{n}} \approx -\frac{1}{q}\nabla(-q.\mu_{\text{n}}.n\nabla\phi + q.D_{\text{n}}\nabla n). \tag{3.20}$$

The diffusion coefficient and electron mobility are related by the Einstein relation [16]:

$$\mu_{\text{n}} = \frac{q}{k_{\text{B}}T}D_{\text{n}}. \tag{3.21}$$

Utilizing the Boltzmann approximation [16], the electron density n can be expressed as:

$$n = N_{\text{C}} \cdot \exp\frac{E_{\text{fn}} - E_{\text{C}}}{k_{\text{B}}T}. \tag{3.22}$$

Applying equations 3.6, 3.21 and 3.22, the equation 3.20 can be rewritten as:

$$\nabla(n\mu_{\text{n}}\nabla E_{\text{fn}}) = qR_{\text{n}}. \tag{3.23}$$

This represents the simplified version of the electron drift-diffusion equation, where the dependent variable is E_{fn} quasi-Fermi level energy.

3.2.2 Flux term (tunneling)

The flux term in this simplified electron drift-diffusion equation accounts for the recombination rate of tunneling in the z direction (where z signifies the direction along the length of the 1D model). The electron recombination rate is given by:

$$R_{\mathrm{n}} = \frac{4.m_{\mathrm{eff}}.\pi}{h^3} N_{\mathrm{sup}}(E_{\mathrm{z}}) TC(E_{\mathrm{z}}) \frac{\mathrm{d}E}{\mathrm{d}z}. \tag{3.24}$$

Here, $\frac{\mathrm{d}E}{\mathrm{d}z}$ represents the energy derivative in the z direction, and E_{z} is the energy in the z direction. The supply function N_{sup} is defined as the difference between Fermi-Dirac distributions on the two sides of the interface:

$$N_{\mathrm{sup}} = k_{\mathrm{B}}.T \ln\left(\frac{1+\exp(-\frac{E_{\mathrm{z}}-E_{\mathrm{fn},1}}{k_{\mathrm{B}}.T})}{1+\exp(-\frac{E_{\mathrm{z}}-E_{\mathrm{fn},2}}{k_{\mathrm{B}}.T})}\right). \tag{3.25}$$

Here the $E_{\mathrm{fn},1}$ and $E_{\mathrm{fn},2}$ are Fermi levels at the two sides of the interface.
The transmission probability TC can be evaluated as:

$$TC(E_{\mathrm{z}}) = \exp\left(-\frac{2}{\hbar}\int_0^{z_0} \sqrt{2.m_{\mathrm{eff}}(E_{\mathrm{z0}} - E_{\mathrm{z}})}\mathrm{d}z\right). \tag{3.26}$$

where $\hbar$ is the reduced Planck's constant, and z_0 is the point at which the electron's energy is to E_{z}. A sketch of the tunneling mechanism through the potential barrier at the metal-oxide interface is shown in Figure 3.4.

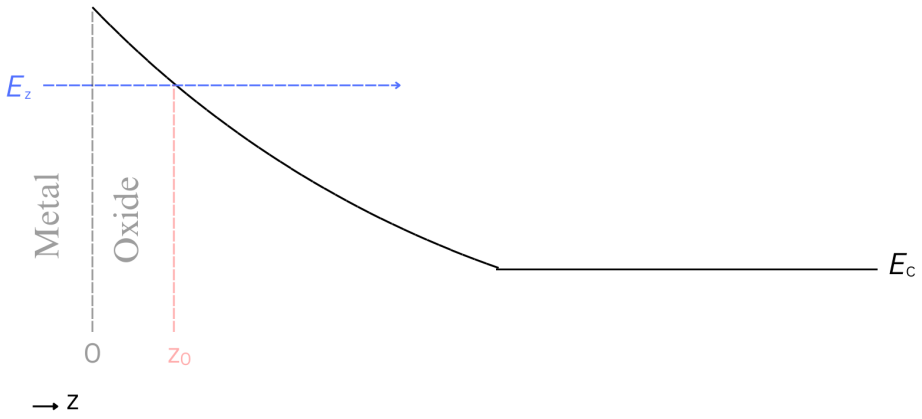

Figure 3.4: Sketch of tunneling mechanism through the potential barrier at the metal-oxide interface.

Having Equation 3.23, the current density can be expressed as the gradient of the quasi-Fermi level:

$$J = \mu_{\mathrm{n}} n \nabla E_{\mathrm{fn}}. \tag{3.27}$$

A more detailed explanation is provided at Gehring's work [26].

3.2.3 Direct tunneling

One can determine the current resulting from direct tunneling, which occurs between two oxide layers. When two oxide or semiconductor layers come into contact, similar to Schottky contacts, their Fermi-level energies tend to align, causing a discontinuity in the conduction band. An illustration of this discontinuity is provided in Figure 3.5.

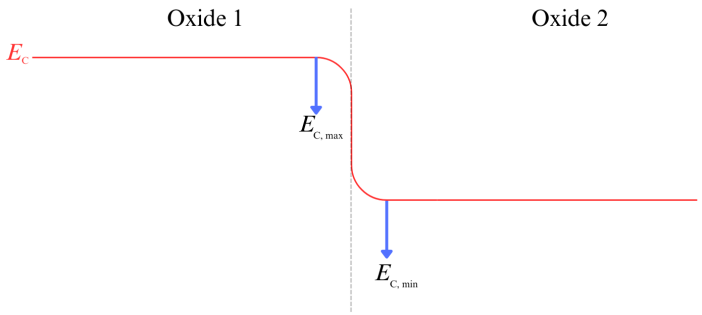

Figure 3.5: Schematic of conduction band energy at oxide-oxide interface.

This discontinuity results in an energy barrier and electrons may tunnel through and by that overcome this barrier and generate a current. This current density can be calculated as outlined in Subsection 2.3.3:

$$J_{\text{direct}} = \frac{4\pi m_{\text{eff}} q}{h^3} \int_{E_{\text{C,min(oxide2)}}}^{E_{\text{C,max(oxide1)}}} TC(E_z) N_{\text{sup}}(E_z) \mathrm{d}E_z. \tag{3.28}$$

Here, $E_{\text{C,max}}$ and $E_{\text{C,min}}$ represent the maximum and minimum values of the conduction band energy around the barrier, i.e., the conduction band energy in oxide 1 and oxide 2. The supply function and transmission probability are determined using the same equations as discussed in Subsection 3.2.2.

3.2.4 Boundary conditions

To establish the boundary conditions, one can initialize the quasi-Fermi level with specific values. For computational simplicity, setting the initial value of the quasi-Fermi level to zero is a common choice. In this approach, the quasi-Fermi level at the top electrode is set to $-qV_{\text{app}}$ (the negative sign is used since the electron Fermi level is under consideration), while at the bottom electrode, it is set to 0:

$$E_{\text{fn,top}} = -qV_{\text{app}}. \tag{3.29}$$

$$E_{\text{fn,bottom}} = 0. \tag{3.30}$$

In Figure 3.6, a schematic illustrating the applied boundary condition for electron drift diffusion equation is presented.

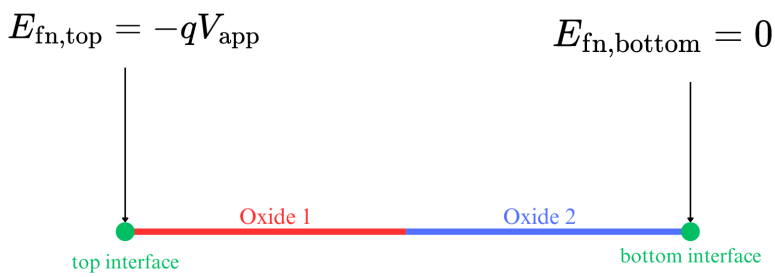

Figure 3.6: Position and value of the parameters used as boundary conditions in electron continuity equation.

3.3 Ion continuity equation

Ions, similar to electrons, are governed by a drift-diffusion equation. As previously discussed, considering only the doubly ionized oxygen vacancies, the drift-diffusion equation for ions can be expressed as:

$$\frac{\partial V_{\ddot{\text{O}}}}{\partial t} - \frac{1}{2q}\nabla(2q.\mu_{V_{\ddot{\text{O}}}}.V_{\ddot{\text{O}}}\nabla\phi + 2q.D_{V_{\ddot{\text{O}}}}\nabla V_{\ddot{\text{O}}} - 2q.V_{\ddot{\text{O}}}.D_{TV_{\ddot{\text{O}}}}\nabla T) = -R_{V_{\ddot{\text{O}}},2}. \tag{3.31}$$

In this equation, $V_{\ddot{\text{O}}}$ is the concentration of the doubly ionized oxygen vacancy and is the dependent variable, while $\frac{\partial V_{\ddot{\text{O}}}}{\partial t}$ is the oxygen vacancy flux. Also $\mu_{V_{\ddot{\text{O}}}}$ represent the oxygen vacancy mobility and $D_{TV_{\ddot{\text{O}}}}$ is the thermal diffusion coefficient of the oxygen vacancy. $R_{V_{\ddot{\text{O}}},2}$ is the total recombination rate of oxygen vacancy and it can be out equal to zero.
Again, with the neglect of the temperature gradient concerning other gradients and using the relationship between mobility and diffusion coefficient, Equation 3.31 will be transformed into:

$$\nabla(-D_{V_{\ddot{\text{O}}}}\nabla V_{\ddot{\text{O}}} - (-\frac{D_{V_{\ddot{\text{O}}}}q}{k_{\text{B}}T}(-\nabla\phi)V_{\ddot{\text{O}}})) + \frac{\partial V_{\ddot{\text{O}}}}{\partial t} = 0. \tag{3.32}$$

This is the simplified oxygen vacancy continuity equation. Here, $-\nabla\Phi$ represents the electric field, and $D_{V_{\ddot{\text{O}}}}$ is the oxygen vacancy diffusion coefficient, which can be determined as:

$$D_{V_{\ddot{\text{O}}}} = D_0 \exp(-\frac{W_{\text{A}}}{k_{\text{B}}T}). \tag{3.33}$$

Here, D_0 is the pre-factor for the maximum diffusion coefficient (at infinite temperature), and W_{A} is the migration barrier height for oxygen ionization, with both parameters dependent on the oxide material. For a more detailed explanation of oxygen ionization, refer to [12].
Implementing boundary conditions for the oxygen vacancy continuity equation involves ensuring that there is no ion exchange at the metal-oxide interface, resulting in the flux terms being set to zero at interface towards the metal material.

$$\hat{n}_{\text{top}}.(-D_{V_{\ddot{\text{O}}}}\nabla V_{\ddot{\text{O}}} - (-\frac{D_{V_{\ddot{\text{O}}}}q}{k_{\text{B}}T}(-\nabla\phi)V_{\ddot{\text{O}}})) = 0. \tag{3.34}$$

$$\hat{n}_{\text{bottom}}.(-D_{V_{\ddot{O}}}\nabla V_{\ddot{O}} - (-\frac{D_{V_{\ddot{O}}}q}{k_{\text{B}}T}(-\nabla\phi)V_{\ddot{O}})) = 0. \tag{3.35}$$

Here $\hat{n}_{\text{top}}$ and $\hat{n}_{\text{bottom}}$ are normal vectors at top electrode and bottom interface pointing towards the electrodes. Hence, they have the coordinates as:

$$\hat{n}_{\text{top}} = (0, 0, -1). \tag{3.36}$$

$$\hat{n}_{\text{bottom}} = (0, 0, 1). \tag{3.37}$$

Also the terms $(-D_{V_{\ddot{O}}}\nabla V_{\ddot{O}} - (-\frac{D_{V_{\ddot{O}}}q}{k_{\text{B}}T}(-\nabla\phi)V_{\ddot{O}})$ represent the flux term of the oxygen vacancy continuity equation and can be represented by $\hat{J}_{V_{\ddot{O}}}$. Therefore, the boundary conditions for the oxygen vacancy continuity equation can be written as:

$$\hat{n}_{\text{top}}.\hat{J}_{V_{\ddot{O}}} = 0. \tag{3.38}$$

$$\hat{n}_{\text{bottom}}.\hat{J}_{V_{\ddot{O}}} = 0. \tag{3.39}$$

In Figure 3.7, a schematic illustrating the applied boundary condition for oxygen vacancy continuity equation is presented.

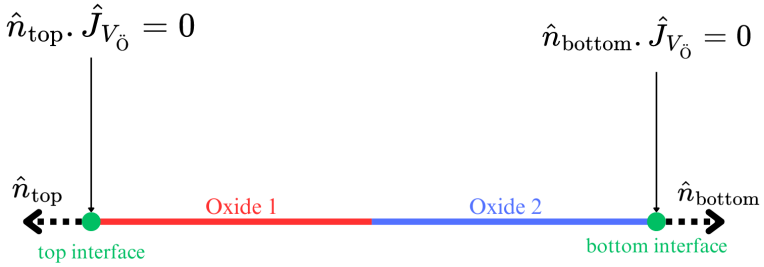

Figure 3.7: Position and value of the parameters used as boundary conditions in ion drift-diffusion equation.

3.4 Heat conduction equation

The fourth differential equation that can be numerically solved is the heat conduction equation, derived from the principles of Joule heating:

$$\nabla(-\kappa\nabla T) = j(-\nabla\phi). \tag{3.40}$$

Joule heating, also referred to as the heating resulting from the flow of electric current, is characterized by the thermal conductivity κ, the total current density j, and the electric field represented by $-\nabla pPhi$. In this equation, the temperature T serves as the dependent variable, and the focus of the simulation is on the study of Joule heating in oxide regions.

The model employs the steady-state formulation of the heat conduction equation, as the equilibrium states of electrons and the lattice are achieved more rapidly compared to the time scales of ionic drift and diffusion.
Ambient temperature is employed as the boundary condition for the heat conduction equation at both the top and bottom electrodes.

$$T_{\text{top}} = T_{\text{environment}} \tag{3.41}$$

$$T_{\text{bottom}} = T_{\text{environment}} \tag{3.42}$$

In Figure 3.8, a schematic illustrating the applied boundary condition for Joule heating equation is presented.

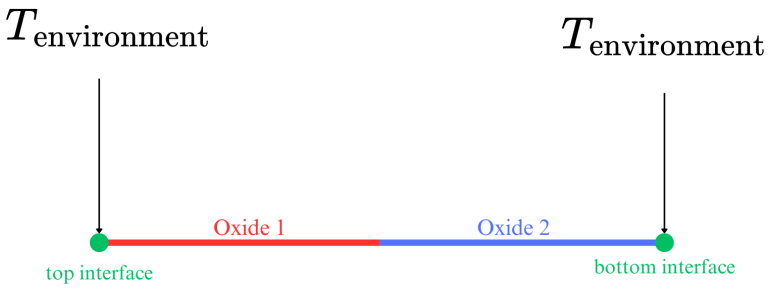

Figure 3.8: Position and value of the parameters used as boundary conditions in heat conduction equation.

Chapter 4

Simulations

In this chapter, simulations are conducted to investigate the behavior of VCM Resistive Random-Access Memory (RRAM) devices. These simulations, based on a rigorous physical model, aimed to uncover the complex mechanisms underlying resistive switching phenomena in VCM ReRAMs. By systematically varying parameters such as applied voltages, pulse time, and others, the simulations provided valuable insights into device performance. Results were analyzed to understand oxygen vacancy dynamics, conduction band energy profiles, and current-voltage characteristics.

4.1 Phase I-a

In the initial phase of the simulation, pulsed voltages are applied to the VCM bi-layer contacts using the parameters outlined in Table 4.1. The simulation utilizes the equations presented in Chapter 3, and a COMSOL project is created based on the formulation of the four differential equations without employing any built-in physics of the COMSOL software.
The applied voltages on the top electrode exhibit pulsed behavior, and the results are collected after the pulses conclude. A schematic depicting of the applied voltage behavior used in this phase is illustrated in Figure 4.1.
The pulsed signal is investigated for both positive and negative polarity, with amplitudes from -2 V to $+2$ V.
The objective of this study is to comprehend the impact of the polarity and amplitude of the external voltage on the distribution of oxygen vacancies along the oxide layers. Alterations in the distribution of oxygen vacancies can potentially influence the conductivity of the VCM cell.
As reported in Appendix A, the temperature changes are insignificant, hence, in further studies results regarding the temperature are not reported.

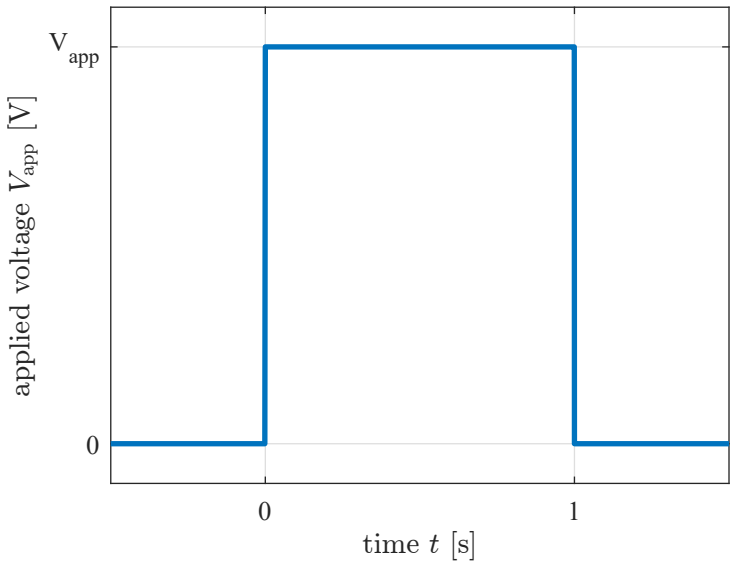

Figure 4.1: $V_{\mathrm{app}}(t)$ - Applied voltage function for simulation phase I-a. The increase and decrease of the voltage happens in a short time (10^{-5} s).

Parameter	**Symbol**	**Value**	**Unit**
oxide 1 thickness	t_{oxide1}	2	nm
oxide 2 thickness	t_{oxide2}	5	nm
electron affinity of oxide 1	χ_1	2.4	eV
electron affinity of oxide 2	χ_2	3.8	eV
band gap energy of oxide 1	E_{g1}	5.8	eV
band gap energy of oxide 2	E_{g2}	4.4	eV
relative permittivity of oxide 1	ϵ_{r1}	22	
relative permittivity of oxide 2	ϵ_{r2}	20	
thermal conductivity of oxide 1	κ_1	1	W/(m·K)
thermal conductivity of oxide 2	κ_2	1	W/(m·K)
electron mobility of oxide 1	μ_{n1}	5	$\mathrm{cm}^2/(\mathrm{Vs})$
electron mobility of oxide 2	μ_{n2}	10	$\mathrm{cm}^2/(\mathrm{Vs})$
effective electron mass for oxide 1	$m_{\mathrm{eff,n1}}$	$0.9 \cdot m_{\mathrm{e}}$	kg
effective electron mass for oxide 2	$m_{\mathrm{eff,n2}}$	$1.7 \cdot m_{\mathrm{e}}$	kg
initial density of donor dopants for oxide 1	N_{D1}	$1 \cdot 10^{16}$	$1/\mathrm{cm}^3$
initial density of donor dopants for oxide 2	N_{D2}	$1 \cdot 10^{20}$	$1/\mathrm{cm}^3$
diffusion coefficient pre-factor for oxide 1	D_{01}	$1 \cdot 10^{-7}$	cm^2/s
diffusion coefficient pre-factor for oxide 2	D_{02}	$1 \cdot 10^{-7}$	cm^2/s
oxygen ion activation energy for oxide 1	W_{A1}	0.5	eV
oxygen ion activation energy for oxide 2	W_{A2}	0.5	eV
top electrode metal work function	$W_{\mathrm{M,top}}$	5.2	eV
bottom electrode metal work function	$W_{\mathrm{M,bottom}}$	4	eV

Table 4.1: Parameters used in simulation (m_{e} denotes the electron mass).

4.1.1 Oxygen vacancy concentration

The initial outcome to analyze following the application of an external voltage for one second to the VCM structure is the oxygen vacancy concentration ($V_{\ddot{O}}$). As detailed in Section 3.3, this variable is the subject of the simplified continuity Equation 3.32.
Figure 4.2 illustrates the distribution of oxygen vacancies along the z axis in the two oxides after the completion of the pulsed voltage application. Notably, even in the absence of an external voltage, there is movement of the oxygen vacancies attributable to the diffusion components of the continuity equation. The plot reveals that applying a positive voltage to the top electrode leads to a reduction in the concentration of oxygen vacancies in oxide 1, with the distribution in oxide 2 remaining relatively unchanged. Conversely, the application of a negative biased voltage increases the density of oxygen vacancies in oxide 1 while leaving oxide 2 more or less unaffected. This observation indicates that the polarity of the applied voltage dictates the direction of the shift in the oxygen vacancy distribution profile.

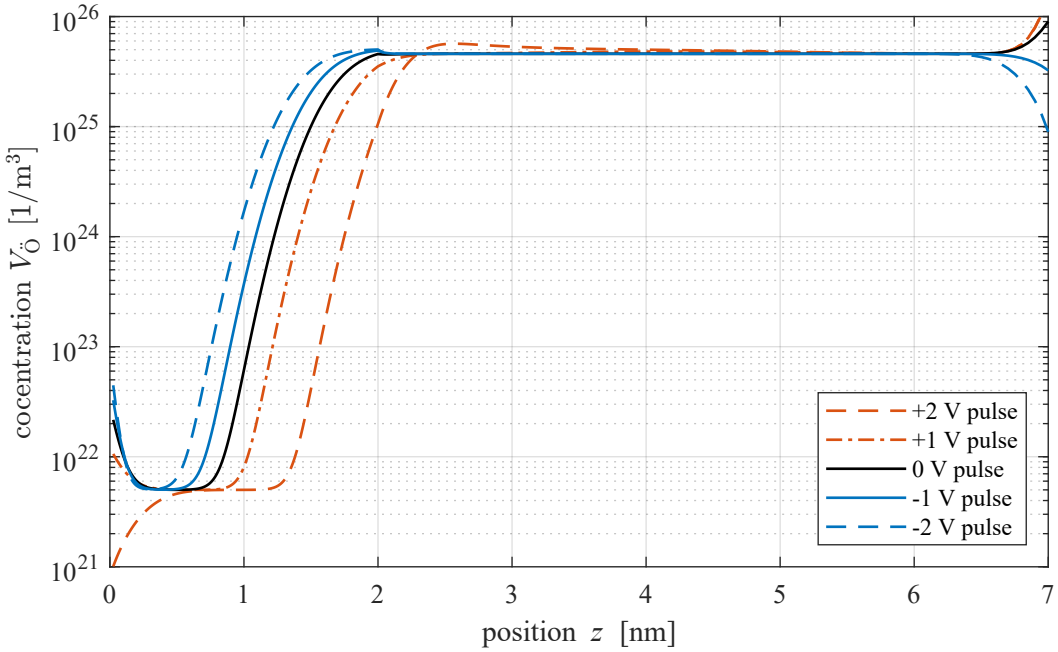

Figure 4.2: $V_{\ddot{O}}(z)$ - Oxygen vacancy concentration along the bi-layer ReRAM cell. The black line represents the condition without applied voltage, the orange lines depict the scenario with positive voltage application, and the blue lines illustrate the effect of negative voltage pulses. Due to the simulation geometry, $z < 2$ nm corresponds to oxide 1 (HfO_x), and $z > 2$ nm represents oxide 2 (TaO_x) areas.

Subsequently, the impact of the amplitude of the externally applied voltage pulse on the oxygen vacancy concentration distribution can be examined. Figure 4.3 presents a comparison of the changes in oxygen vacancy concentration in oxide 1 following the application of various positive voltage pulses. Noticeably, an increase in the amplitude of the positive bias stimuli results in a progressively smaller oxygen vacancy concentration compared to the equilibrium case.
Similarly, the anticipated effect is expected to be present in cases involving negative voltage pulses. Figure 4.4 provides a comparison of different amplitudes of applied negative voltage pulses to the top electrode against the equilibrium case. As evident from the figure, an increase in the amplitude of the negative voltage pulse leads to a higher concentration of oxygen vacancy within oxide 1 compared to

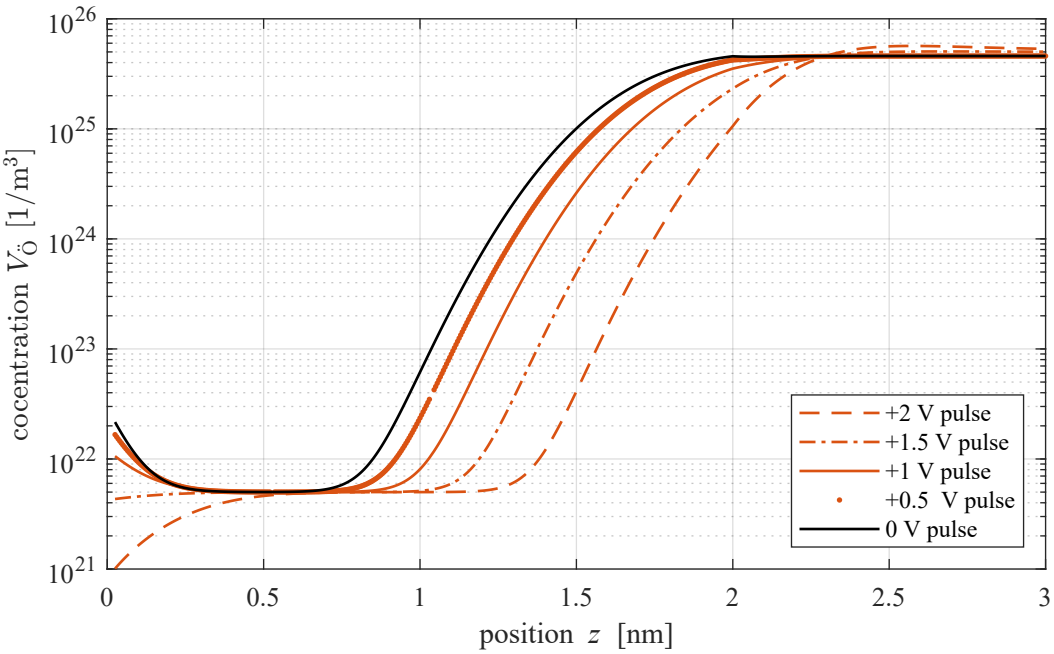

Figure 4.3: $V_{\ddot{O}}(z)$ - Oxygen vacancy concentration along the bi-layer ReRAM cell. The diagram is zoomed in to observe details near and inside the oxide 1 regions. The black line represents the equilibrium case (without external voltages), and the orange lines depict the oxygen vacancy distribution after applying different amounts of positive voltage pulses.

the equilibrium state.

Hence, the influence of application of pulsed voltages on the oxygen vacancy concentration is observed in both positive and negative bias scenarios. These alterations in ionized oxygen vacancies are expected to influence the conductivity of the ReRAM structure.

4.1.2 Conduction band energy

The second parameter of interest in the pulsed input simulation is the conduction band edge energy (E_C). As discussed in Section 3.1, the conduction band energy is determined after solving the Poisson equation and finding the potential. It also depends on the electron affinity of the oxide, as indicated by Equation 3.6. The conduction band energy profile plays a crucial role in the conductivity of the VCM cell, as it influences the number of electrons (charge carriers) according to Equation 3.4.

Figure 4.5 illustrates the conduction band energy along the z axis after the application of different positive voltage pulses. This graph reveals the relationship between the amplitude of the external positive voltage applied to the top electrode and the conduction band energy in the two oxides. As observed in the plot, only the application of +0.5 V leads to a meaningful change in the conduction band energy, resulting in a decrease in the energy of the conduction band. No other amplitude of positive voltage had a significant effect on the conduction band energy in the two oxides. This change of behavior for a specific amplitude of voltage is not reasonable and the origins are unknown.

Figure 4.6 displays $E_C(z)$ after the application of negative voltage pulses in comparison to the situation where no voltage is applied to the top electrode. As evident in the plot, applying different negative voltage pulses to the VCM cell does not affect the energy of the conduction band. Consequently, the distribution of E_C remains largely unchanged after the pulse application.

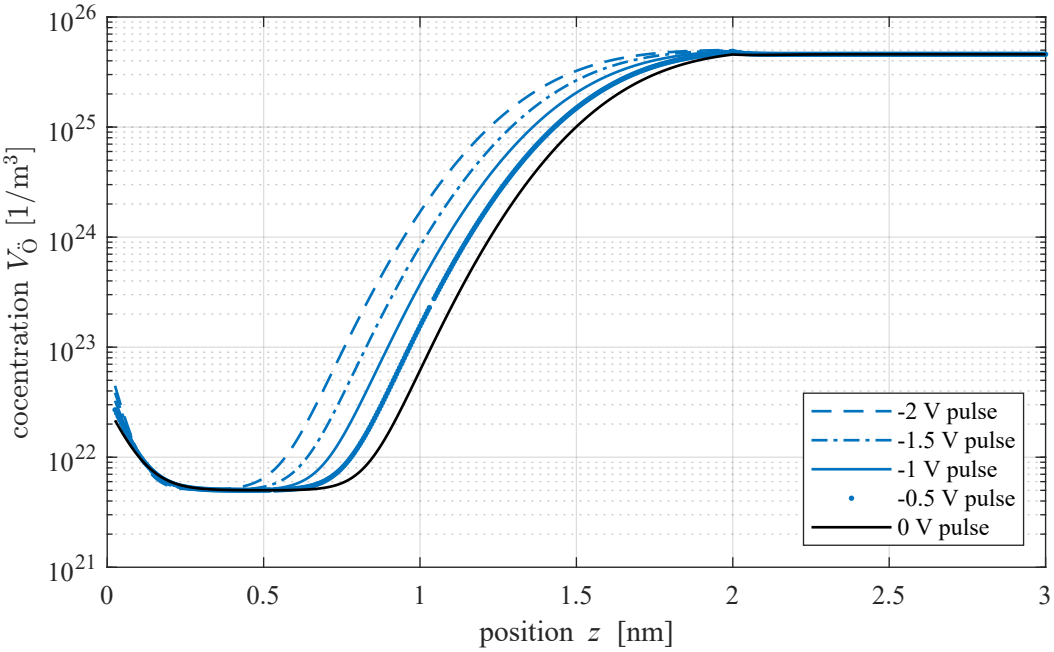

Figure 4.4: $V_{\ddot{O}}(z)$ - Oxygen vacancy concentration along the bi-layer ReRAM cell. The diagram compares different amplitudes of applied negative voltage pulses (blue lines) with the equilibrium case (black line). The diagram concentrates on areas of oxide 1.

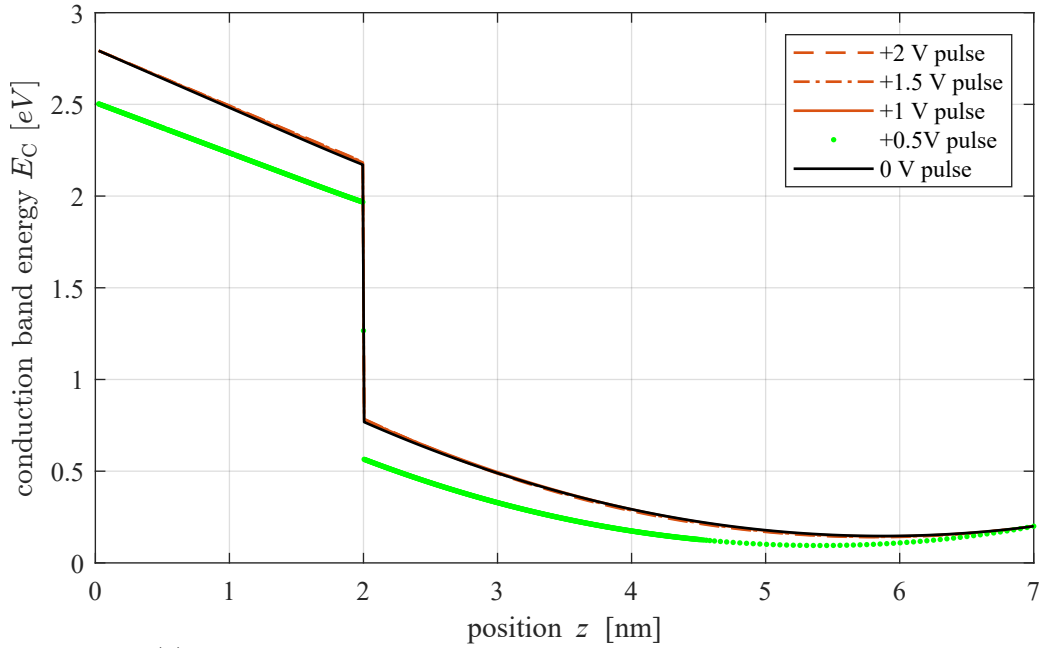

Figure 4.5: $E_C(z)$ - Conduction band energy along the bi-layer VCM cell. The black line represents the energy without the pulsed voltage, orange lines represent the situation after applying positive voltage pulses with no profound change in E_C, and the green line represents the energy for the voltage pulse that has an effect on the conduction band energy level.

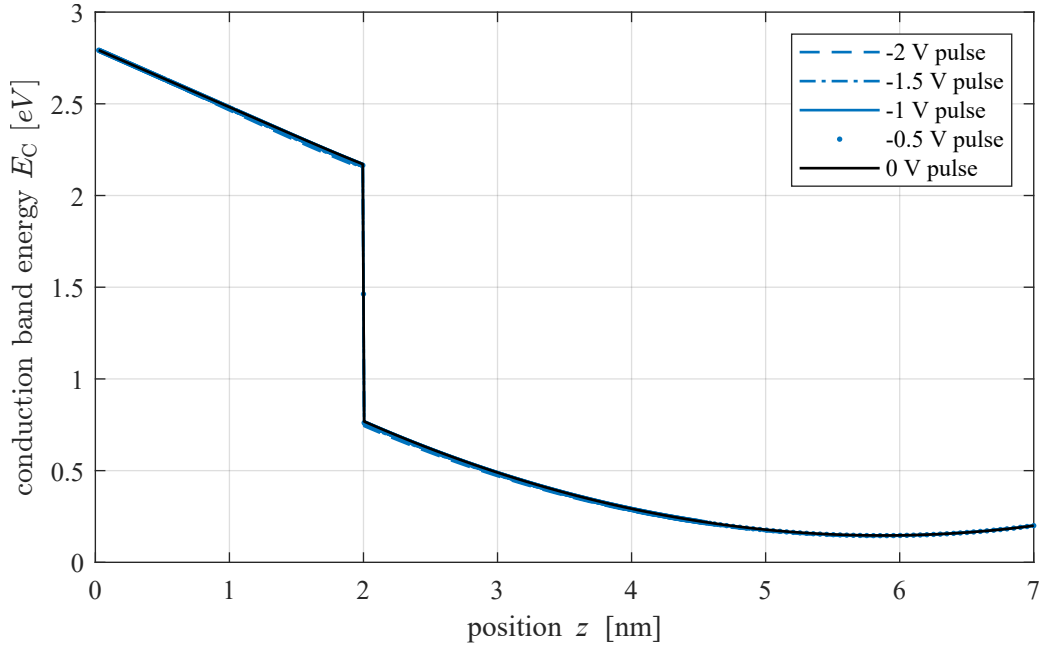

Figure 4.6: $E_C(z)$ - Conduction band energy along the bi-layer VCM cell. The black line represents the energy without the pulsed voltage, blue lines represent the situation after applying negative voltage pulses.

4.2 Phase I-b

In this phase of the simulations, the oxygen vacancy continuity equation is excluded, and the extracted oxygen vacancy distribution ($V_{\ddot{O}}(z)$) from Section 4.1 is utilized. In this step, a range of positive and negative voltages are applied to the previously pulsed VCM layers. Other three main differential equations are still used in the COMSOL project in the same way implemented in Section 4.1 also used parameters are again the ones mentioned in Table 4.1.
Figure 4.7 illustrates the applied voltage on the top electrode in phase I-b as the simulation progresses ($V_{\text{app}}(t)$).
The primary objective of this sweep voltage application after the pulses is to investigate the conductivity of the stack-layer VCM under different oxygen vacancy distributions. In other words, the effect of the ionized oxygen vacancy distribution on the possible resistive switching of the device is studied.

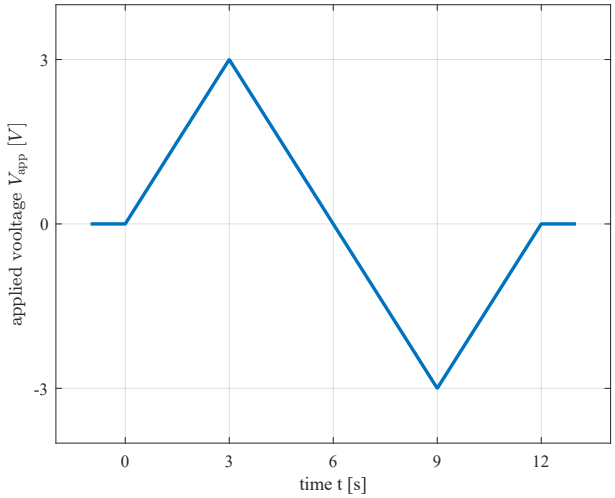

Figure 4.7: $V_{\text{app}}(t)$ - Applied voltage on the top electrode in the time evolution for phase I-b of the simulation.

4.2.1 Current-voltage characteristics

The most crucial outcome to study in this phase is the current density at different applied voltages, i.e., the JV characteristics. The current density can be determined using Equation 3.27, subsequent to finding the electron density and solving the quasi-Fermi level differential equation. This current density (J) can be obtained at each geometrical point in the device. Typically, the maximum current density is observed near the middle of oxide 2. Figure 4.8 shows examples of current density profile in different voltages of the sweep, in all of them middle point of the oxide 2 can be seen as the maximum point. Hence, this point is usually utilized as the reference. In the following results middle of oxide 2 ($z = 4.5$ nm) is chosen as the reference point to measure the current density.
Figure 4.9 illustrates the JV characteristics of the VCM cell subjected to pulses with positive, negative, and zero volts. Firstly, it is evident that the amplitude of the current density is much lower in negative biases compared to positive biases, possibly due to the asymmetric configuration of the stacked layer structure. Secondly, by comparing the current density under different pulsed conditions, it can be observed that although small, applying a negative voltage pulse increases the current density in both positive and negative applied biases. In contrast, applying a positive voltage pulse decreases the current density compared to the case when no pulse is applied to the bi-layer VCM. This difference

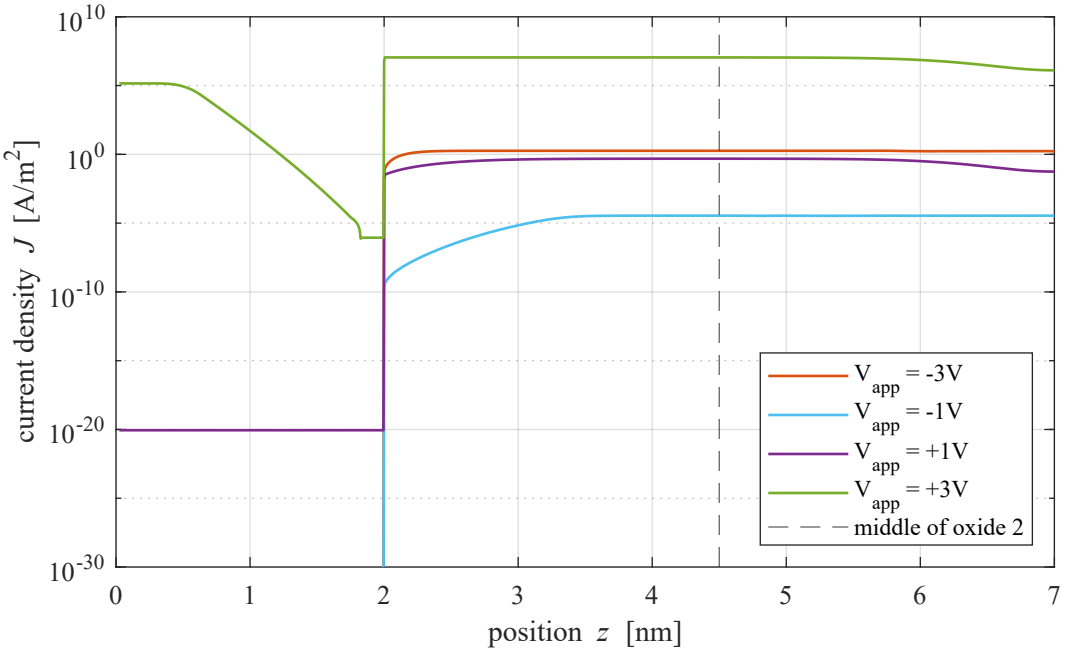

Figure 4.8: $J(z)$ - Current density distribution at different V_{app}, where $z = 4.5$ nm (dashed line) represents the middle of oxide 2.

in JV behavior can be attributed to the alteration in oxygen vacancy distribution resulting from the pulsed signals applied to the top electrode in Section 4.1.

To gain further insights into the influence of pulse voltage on the conductivity of the structure, JV characteristics of the positively pulsed cases can be examined, as illustrated in Figure 4.10. As evident from the plots, further increasing the voltage of the positively pulsed bias leads to a decrease in current density when the VCM is subjected to sweep voltage testing. In other words, applying higher voltages as positive bias pulses results in lower conductance observed in the cell. However, it is important to note that these changes are relatively small.

The behavior observed for negative voltage pulses mirrors that of positive pulses. As depicted in Figure 4.11, increasing the amplitude of negative voltage pulses leads to higher current densities. In essence, applying greater negative voltages during pulse steps enhances conductivity, aligning with the changes in oxygen vacancy distribution following exposure to pulsed voltage in VCM devices.

Indeed, the observed changes in current density suggest a direct correlation between the applied pulsed voltages and the distribution of oxygen vacancies, which serve as charge carriers within the VCM structure. This behavior underscores the significance of oxygen vacancies in modulating the conductivity of the device, as their migration across the oxide layers influences the flow of current under different bias conditions.

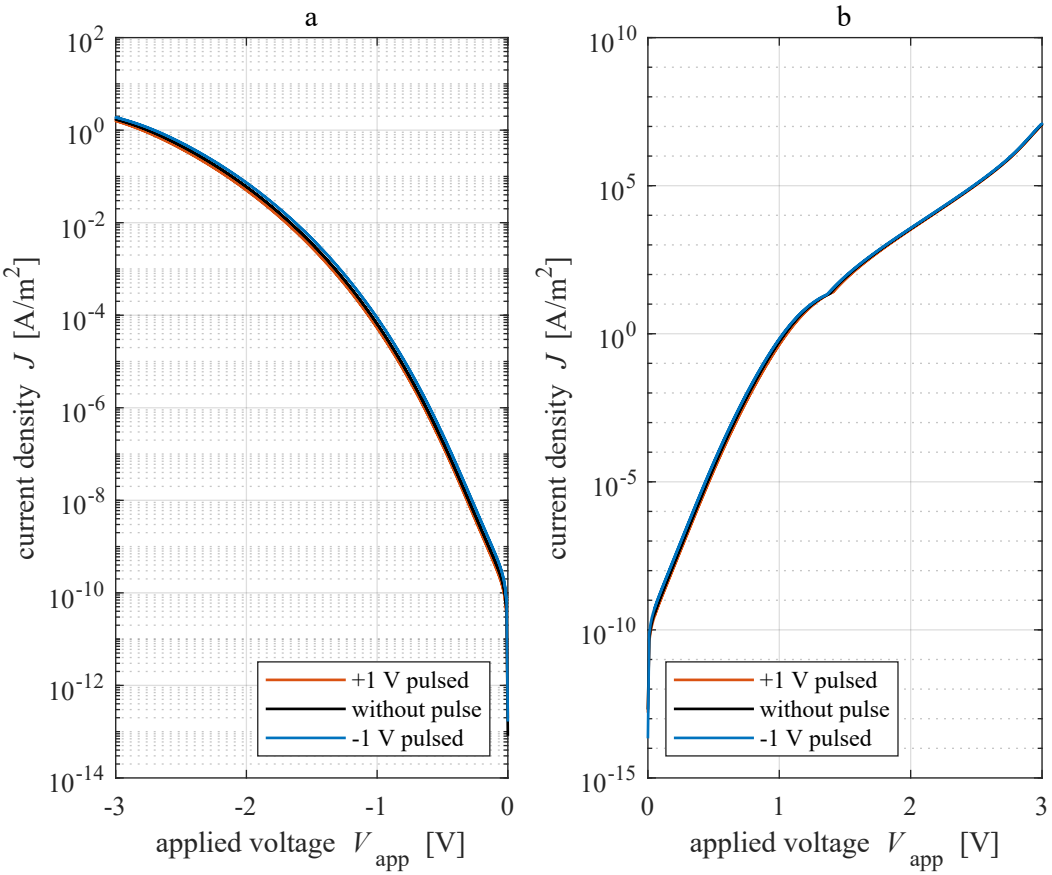

Figure 4.9: JV characteristics of the VCM cell under a) negative voltages and b) positive voltages. The black lines represent the case where no voltage pulse is applied, the blue line shows the current for the case where a -1 V pulse is applied, and the $+1$ V pulse case is depicted with the orange line (all the currents are measured in $z = 4.5$ nm).

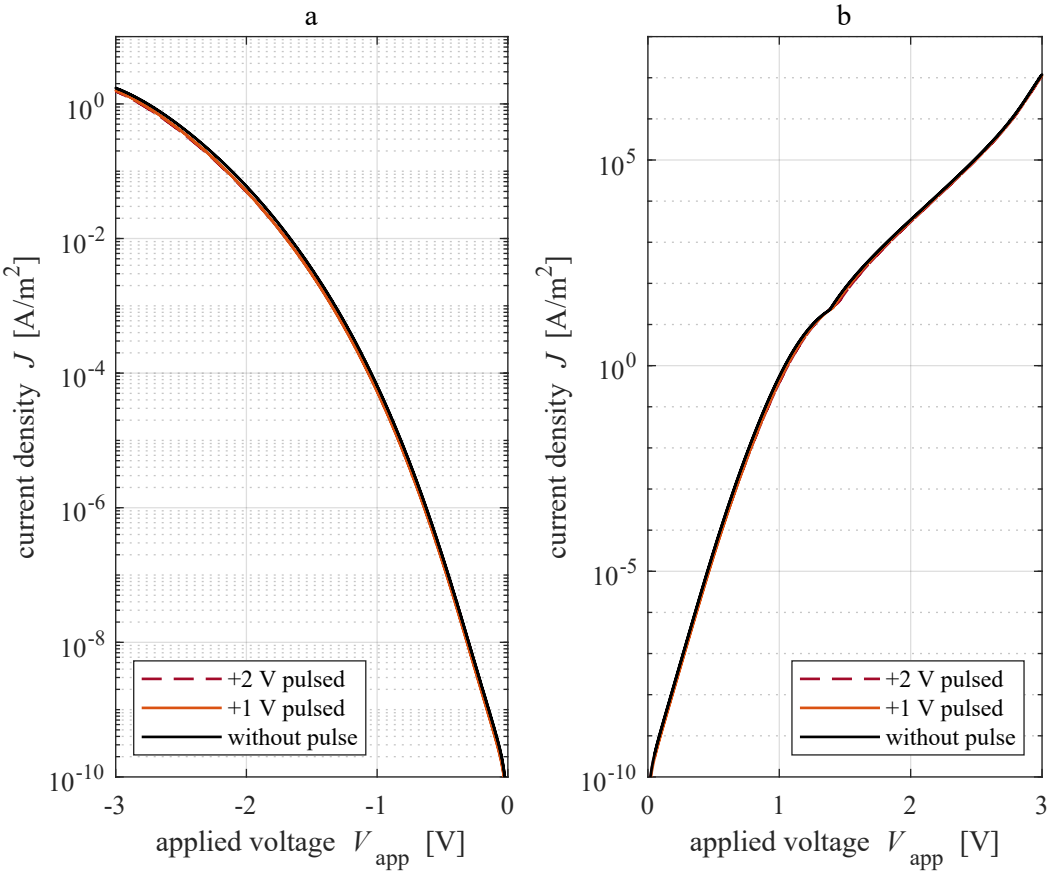

Figure 4.10: JV characteristics of the VCM cell under a) negative voltages and b) positive voltages. The black lines represent the case where no voltage pulse is applied, the orange lines show the current for the cases where a positive pulse is applied (all the currents are measured in $z = 4.5$ nm).

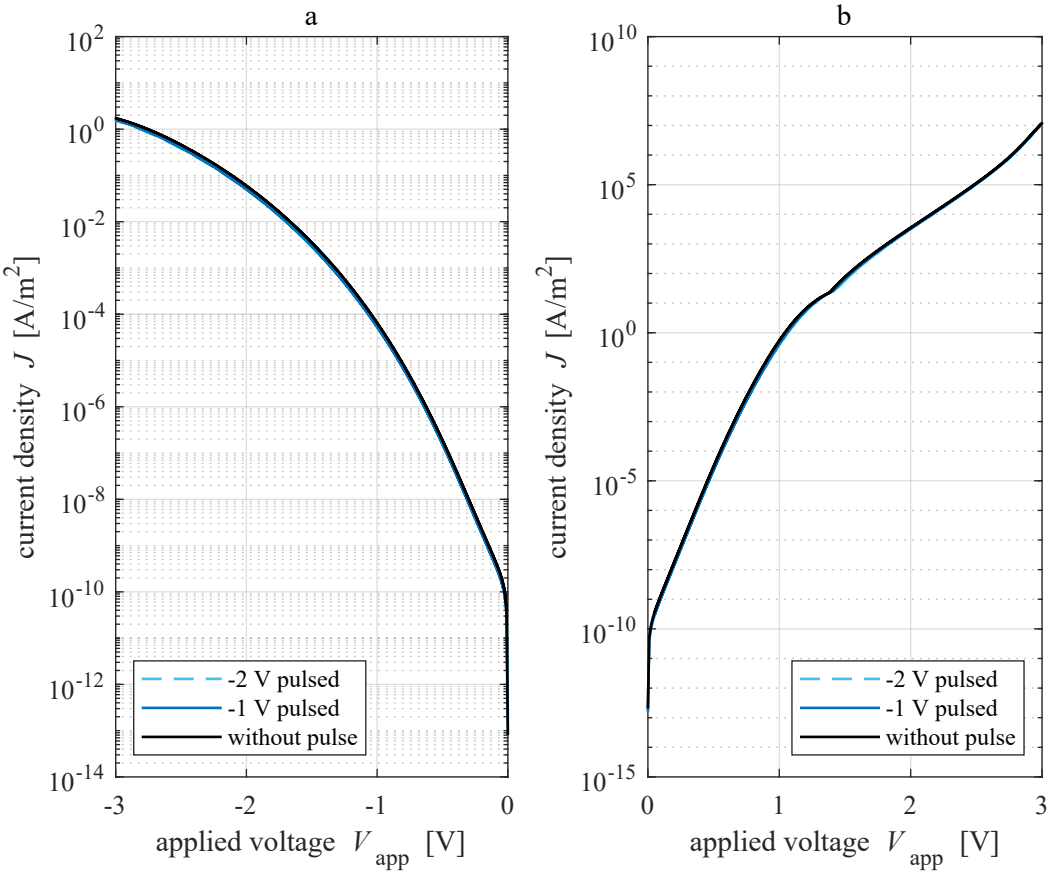

Figure 4.11: JV characteristics of the VCM cell under a) negative voltages and b) positive voltages. The black lines represent the case where no voltage pulse is applied, the blue lines show the current for the cases where a positive pulse is applied (all the currents are measured in $z = 4.5$ nm).

4.3 Phase I-c

In this phase of the study, the focus shifts to understanding the impact of the duration for which voltage is applied to the VCM. Using the same methodology and parameters as in Phase I-a, the duration of the applied pulses is extended to 5 s and 10 s, allowing for a comparison with the results obtained from one second pulses in Section 4.1. Figure 4.12 shows the applied voltage as a function of the simulation time for this phase. By varying the pulse duration, insights can be gained into how the temporal aspect of the voltage application influences the behavior of the VCM device. The used voltages in this phase are: -2 V, -1 V, 0 V, 1 V and 2 V.

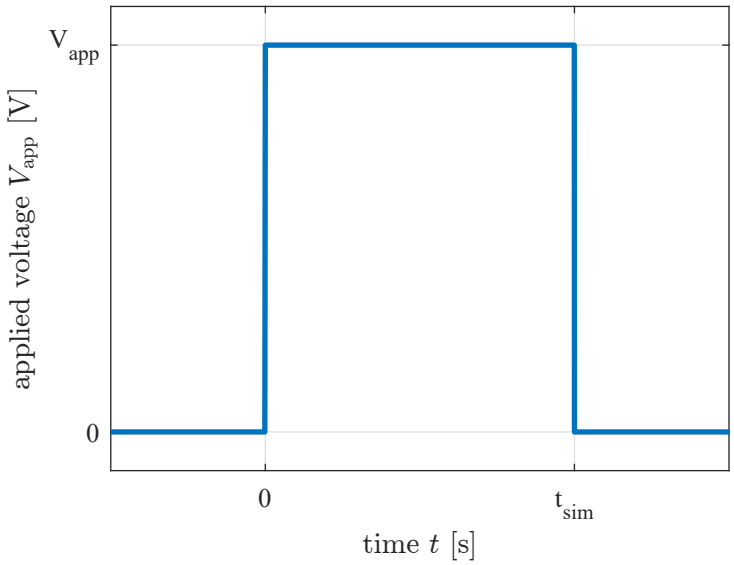

Figure 4.12: $V_{\text{app}}(t)$ - Applied voltage function for simulation phase I-c. The increase and decrease of the voltage happens in a short time (10^{-5} s).

4.3.1 Oxygen vacancy concentration

The initial property to examine following the alteration in pulse duration is the distribution of oxygen vacancy concentration ($V_{\ddot{\text{O}}}(z)$) across the two oxides. As detailed in Subsection 4.1.1, this distribution was previously analyzed for pulse duration of one second. Now, the impact of extending the pulse duration can be investigated to determine any variations in the oxygen vacancy distribution.
To establish a baseline, the impact of time in the absence of a pulsed voltage is examined first. Figure 4.13 illustrates the variation in the oxygen vacancy distribution across the ReRAM structure under the absence of external voltage application, at different simulation times. As depicted in the plot, even without applying any voltage to the top electrode, there is noticeable movement of oxygen vacancies. This movement is primarily driven by the diffusion component of the ion continuity equation (Equation 3.32). With longer simulation times, this phenomenon becomes more pronounced, leading to an increase in the concentration of oxygen vacancies within the oxide 1 region (the region with initially lower concentration).
The subsequent analysis involves examining the influence of pulse voltage duration under positive bias conditions. Figures 4.14 and 4.15 present the spatial distribution of oxygen vacancies at various pulse durations for applied voltages of +1 V and +2 V respectively. The results for the case when the applied pulsed voltage is +1 V reveal that while the positive bias exhibits a reverse effect compared to the duration of the pulse, it does not entirely prevent the increase in oxygen vacancy concentration

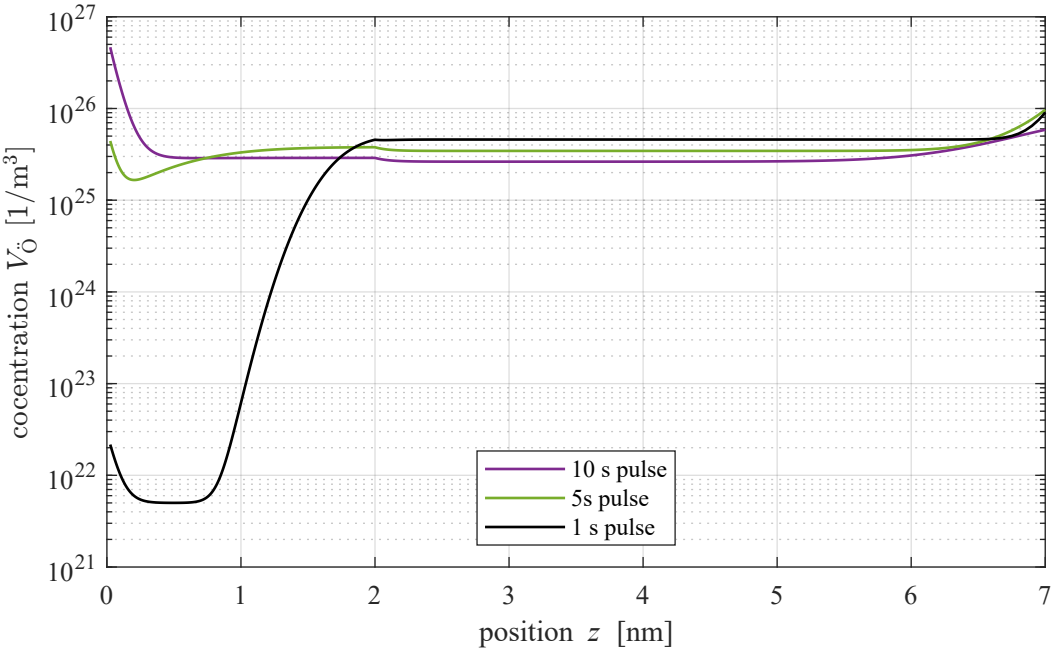

Figure 4.13: Variation of oxygen vacancy concentration ($V_{\ddot{O}}(z)$) across different positions of the VCM structure under an external voltage pulse of 0 V, applied for durations of 1 s (black line), 5 s (green line), and 10 s (purple line).

in the oxide 1 region. However, the increment is lower compared to the scenario without applied bias. Conversely, in the plots corresponding to $V_{\text{app}} = +2$ V, it is evident that a higher magnitude of positive pulsed voltage can counteract the effect of diffusion. With increased pulse duration, the concentration of oxygen vacancies decreases in the oxide 1 regions. This suggests that the magnitude of the positive bias significantly influences the changes in oxygen vacancy distribution along the VCM structure.

In the final comparison, we explore the impact of simulation duration on cases where a negative pulse voltage is applied to the top electrode of the VCM. Figures 4.16 and 4.17 illustrate the oxygen vacancy concentration across the structure in different pulse time durations for -1 V and -2 V pulses, respectively. The results indicate that increasing the duration of the applied negative pulsed voltage leads to a rise in the oxygen vacancy increment in the oxide 1 region. Notably, both negative bias application and longer simulation times produce a similar effect on this property, accelerating the increase in oxygen vacancy concentration compared to scenarios with no applied pulse. Furthermore, with an increase in the magnitude of the negative bias, the reduction in oxygen vacancy concentration in oxide 2 regions becomes more pronounced as the pulse duration increases.

4.3.2 Conduction band energy

The second parameter that warrants examination after applying pulses of varying durations is the conduction band energy ($E_{\text{C}}(z)$). This property, obtained using the methods described in Subsection 4.1.2, is crucial for understanding electrical conduction of the device.

To begin, we analyze the impact of time when no external voltage is applied to the top electrode. Figure 4.18 illustrates the conduction band energy across different regions of the structure. As evident in the plot, increasing the simulation time without any external bias applied to the top electrode leads to a rise in the energy of the conduction band across all regions of the VCM. This change can be

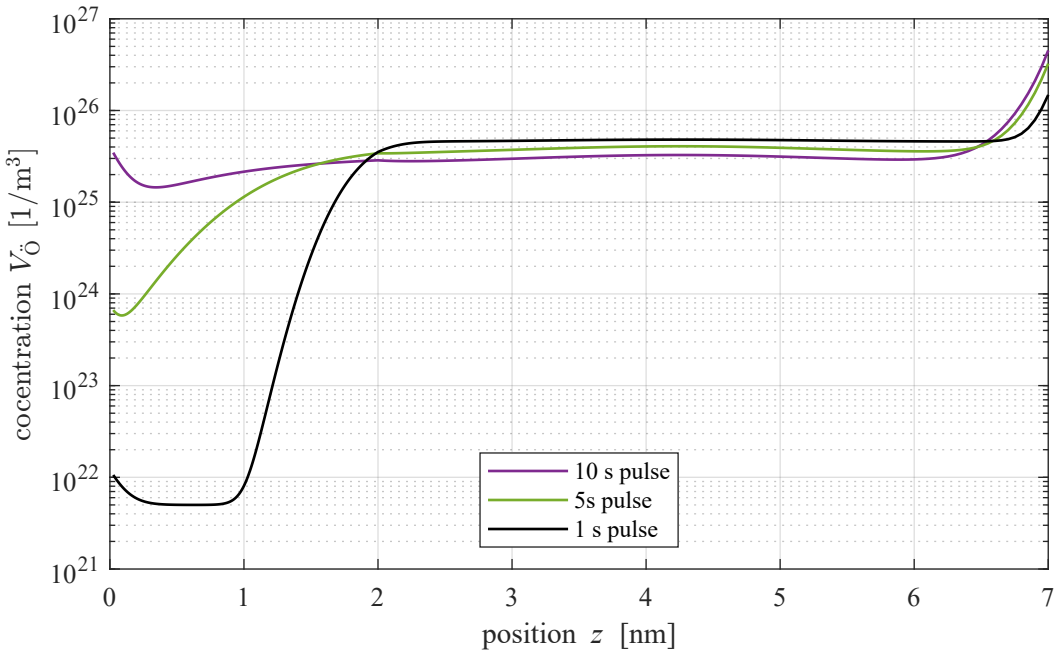

Figure 4.14: Variation of oxygen vacancy concentration ($V_{\ddot{O}}(z)$) across different positions of the VCM structure under an external voltage pulse of +1 V, applied for durations of 1 s (black line), 5 s (green line), and 10 s (purple line).

attributed to the diffusion contribution of the continuity equations utilized in the model.

One can then examine how the conduction band energy changes when an external voltage is applied in the form of a pulse. While the results for a pulse duration of 1 s have been previously discussed in Subsection 4.1.2, it is now valuable to observe the impact of prolonging the pulse duration on the conduction band across the oxide layers. Figure 4.19 illustrates the conduction band at various positions when voltage pulses of different polarities and magnitudes are applied for a duration of 5 s. from the plot, it can be inferred that for an applied voltage magnitude of 1 V, regardless of polarity, the conduction band energy remains relatively stable even as the pulse duration increases to 5 s. However, with a higher voltage amplitude, noticeable changes in the conduction band energy become apparent at this pulse duration. Specifically, for cases with a magnitude of 2 V, there is an increase in the conduction band energy when the pulse polarity is negative, whereas a decrease in E_C is observed when a positively biased voltage is applied.

One can further explore the alterations in the conduction band energy with a longer simulation time of ten seconds. Extending the simulation duration allows for a deeper understanding of how the conduction band evolves across the oxide layers under prolonged voltage pulses. Figure 4.20 illustrates the conduction band at various positions when voltage pulses of different polarities and magnitudes are applied for a duration of 10 s. According to the results depicted in the plot, when the duration of the pulse application is extended to 10 s, its effect on the conduction band energy becomes notably evident. In cases of positive biases, the conduction band energy experiences a decrease, particularly pronounced in oxide 2 regions, and this effect becomes more evident with increasing voltage amplitude. Conversely, for negative biases, there is an increase in the energy level of the conduction band, with this phenomenon being further enhanced when higher magnitudes of negative voltage are used as the pulse.

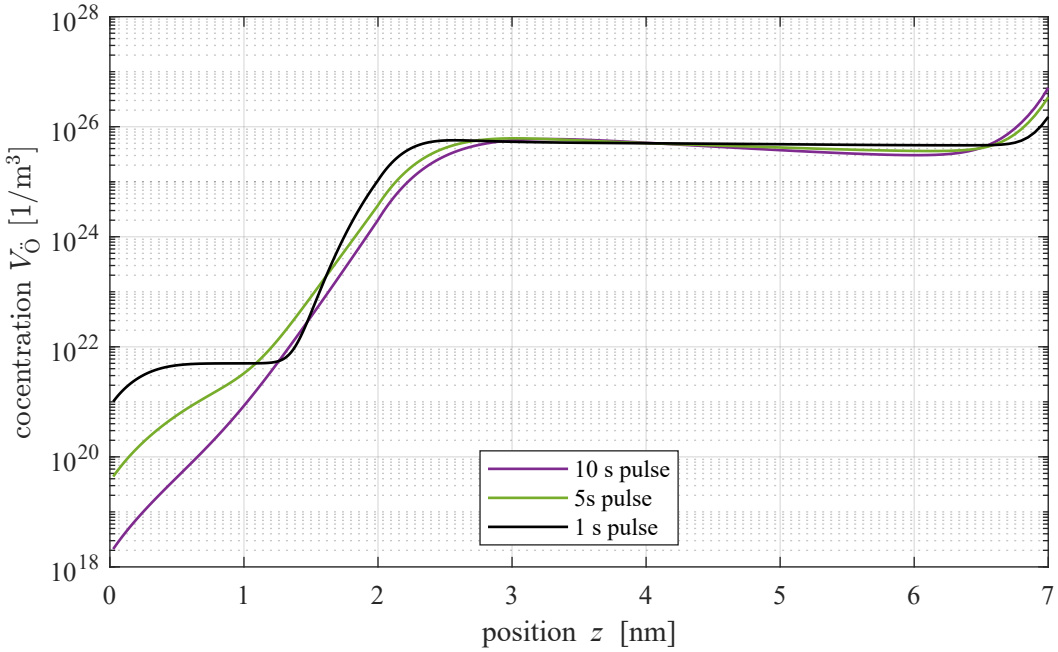

Figure 4.15: Variation of oxygen vacancy concentration ($V_{\ddot{O}}(z)$) across different positions of the VCM structure under an external voltage pulse of +2 V, applied for durations of 1 s (black line), 5 s (green line), and 10 s (purple line).

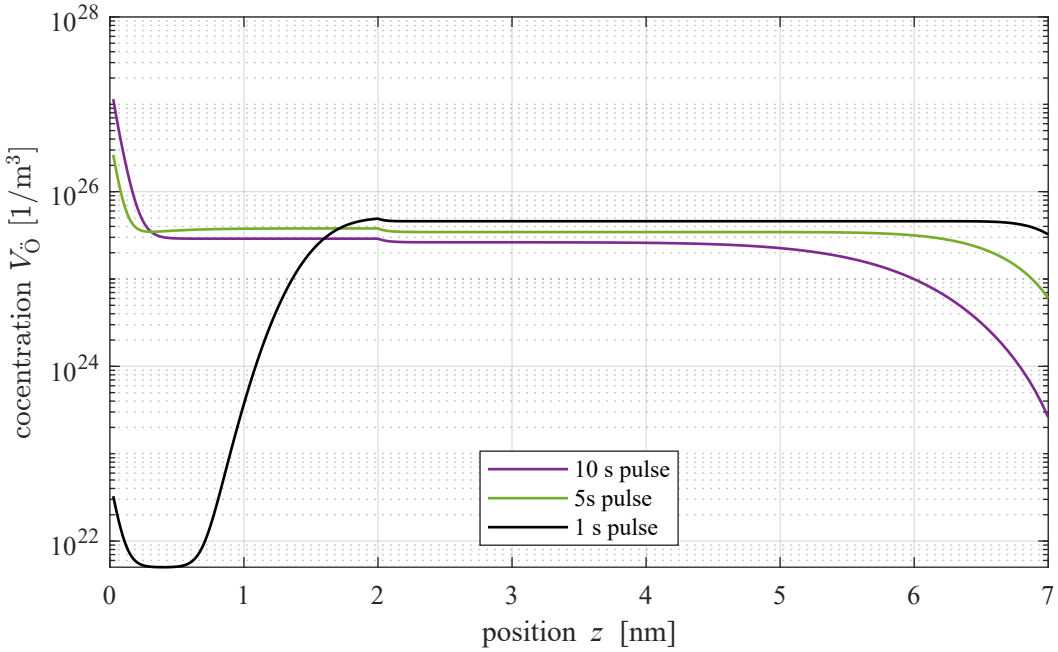

Figure 4.16: Variation of oxygen vacancy concentration ($V_{\ddot{O}}(z)$) across different positions of the VCM structure under an external voltage pulse of −1 V, applied for durations of 1 s (black line), 5 s (green line), and 10 s (purple line).

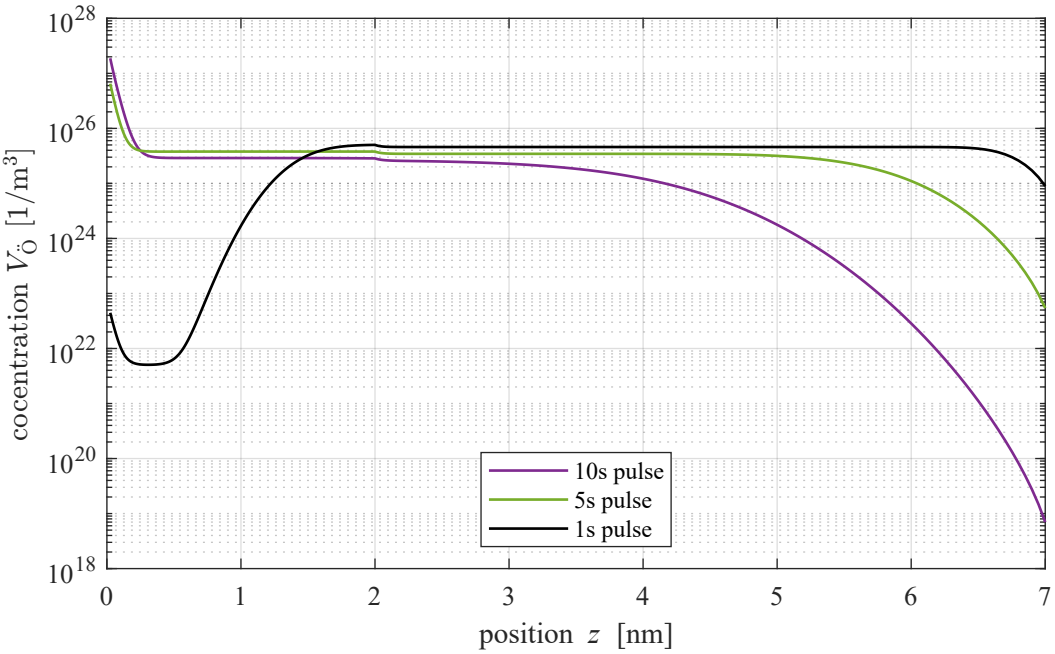

Figure 4.17: Variation of oxygen vacancy concentration ($V_{\ddot{O}}(z)$) across different positions of the VCM structure under an external voltage pulse of -2 V, applied for durations of 1 s (black line), 5 s (green line), and 10 s (purple line).

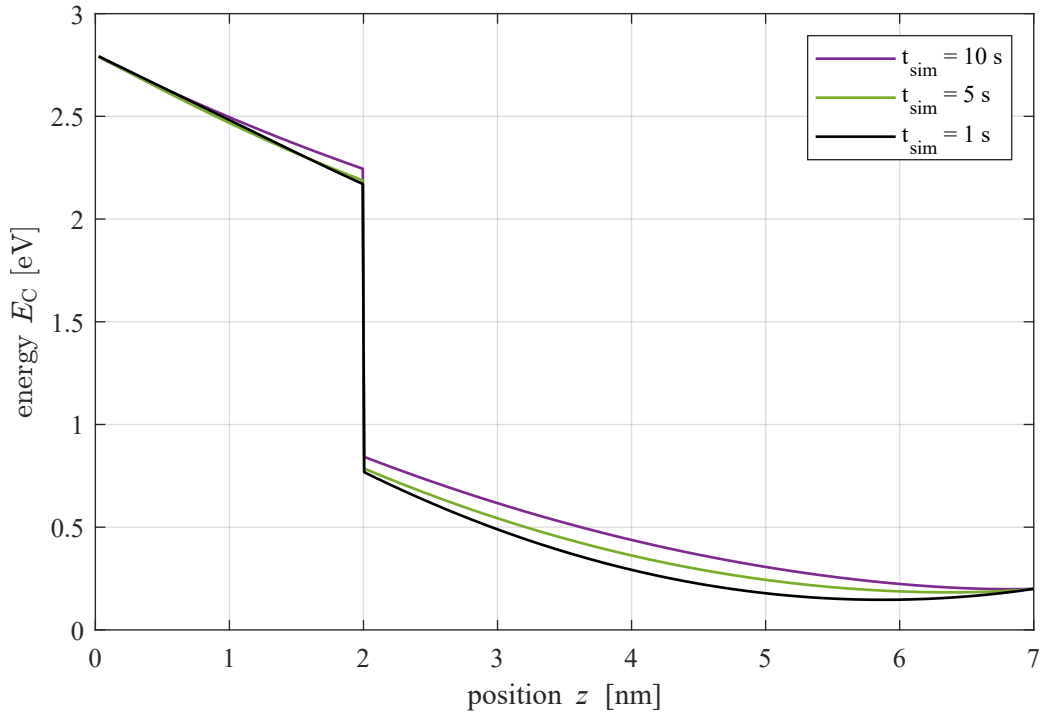

Figure 4.18: $E_C(z)$ - Conduction band energy in various positions of the VCM bi-layer structure at different simulation durations without external bias. The black line represents the 1 s simulation time, the green line corresponds to 5 s duration, and the purple line depicts the 10 s case.

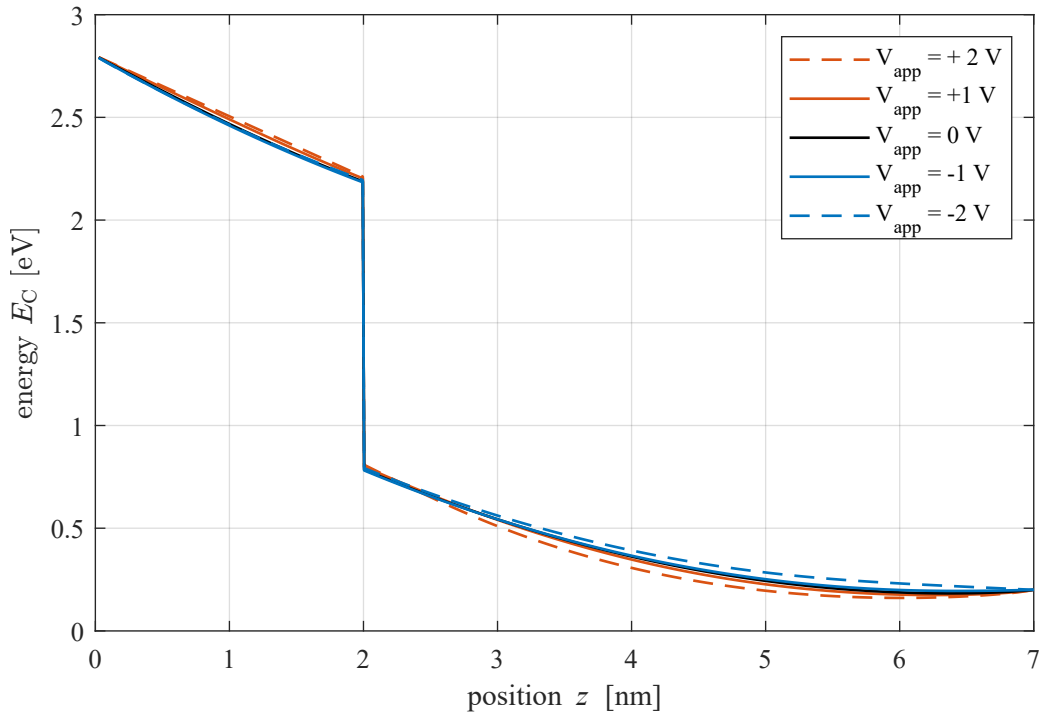

Figure 4.19: $E_C(z)$ - Conduction band energy in various positions of the VCM bi-layer structure at 5 s duration of pulse applied voltage. The black line represents the case without external voltage, the orange lines correspond to positive voltages, and the blue lines depict the case when the applied pulses have negative polarity.

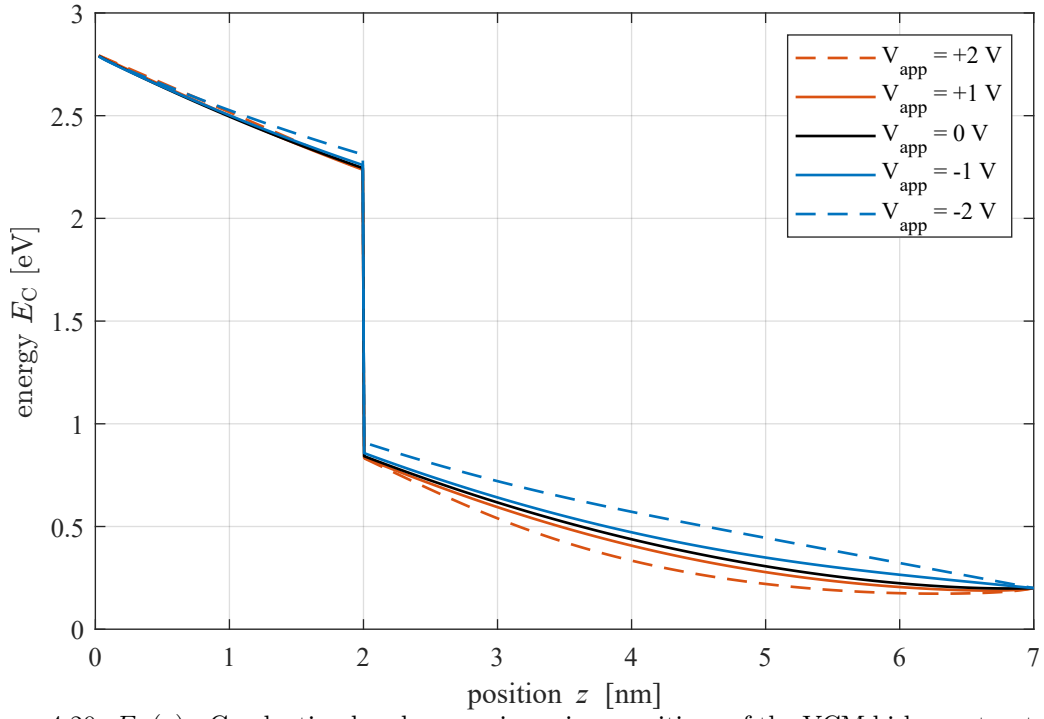

Figure 4.20: $E_C(z)$ - Conduction band energy in various positions of the VCM bi-layer structure at 10 s duration of pulse applied voltage. The black line represents the case without external voltage, the orange lines correspond to positive voltages, and the blue lines depict the case when the applied pulses have negative polarity.

4.4 Phase I-d

In Section 4.3, it was evident that increasing the simulation time without applying any external electrical bias leads to a more equal distribution of oxygen vacancy concentration between oxide 1 and oxide 2 regions. Therefore, it is anticipated that further increases in simulation time will not alter the oxygen vacancy distribution, reaching a relaxed state.

4.4.1 Reaching relaxed state

In this phase of the simulation, the parameters used are detailed in Table 4.1, and the implementation mirrors that of Section 4.3. However, longer simulation times are examined (up to 60 seconds).
Initially, the device undergoes simulation without any voltage pulses for varying durations. Figure 4.21 illustrates the oxygen vacancy distribution after simulating in different times up to one minute without applied voltage. As depicted in the plot, the oxygen vacancy distribution profile continues to evolve with increasing simulation time, even up to one minute. Consequently, a steady state is not attained within the 60-second timeframe. Thus, extending the simulation duration is necessary to reach a relaxed-state profile, in which the mean concentration would not be changed over time.
In Figure 4.22, the changes in oxygen vacancy distribution in the absence of an external voltage are depicted for different durations up to five minutes. As depicted in the plot, after three minutes of simulation time, the oxygen vacancy concentration distribution appears to stabilize, showing little change thereafter. Consequently, this distribution can be considered as the steady-state configuration for further analysis.

4.4.2 Oxygen vacancy in different states

After establishing the equilibrium distribution of oxygen vacancies (relaxed state), it serves as a reference for subsequent steps. As depicted in Figure 4.15, the application of a positive voltage as large as 2 V leads to a decrease in the concentration of oxygen vacancies in the oxide 1 region. To further explore this phenomenon, the relaxed state can be utilized as the initial condition for the oxygen vacancy distribution, followed by the application of a positive voltage to the top electrode. The changes in distribution relative to the relaxed state are then monitored when an external force is applied to the VCM cell.
Figure 4.23 illustrates the mean value of the oxygen vacancy distribution over time when a positive bias of magnitude 2 V is applied, starting from the relaxed state. The plot indicates that applying a positive bias of 2 V to the top electrode results in a decrease in the oxygen vacancy concentration within the oxide 1 region compared to the steady-state concentration. However, it takes some time for the external bias to overcome diffusion effects before the decrement becomes apparent. Also 10 s is not enough to reach the initial concentration for the simulations, before trying to reach relaxed state (from Equation 3.3).
To further explore the alterations of the oxygen vacancy concentration in the oxide 1 region from the steady state under the influence of positive voltage, additional simulation times and various positive voltage magnitudes are investigated.
Figure 4.24 illustrates the fluctuations in the mean value of $V_{\dot{O}}$ in the oxide 1 region for different positive voltage levels over a simulation period of 100 s, all initialized from the steady-state concentration. As depicted in the plot, applying a +1 V bias does not alter the concentration of oxygen vacancies in the first oxide from the steady-state configuration, indicating an inability to overcome the redis-

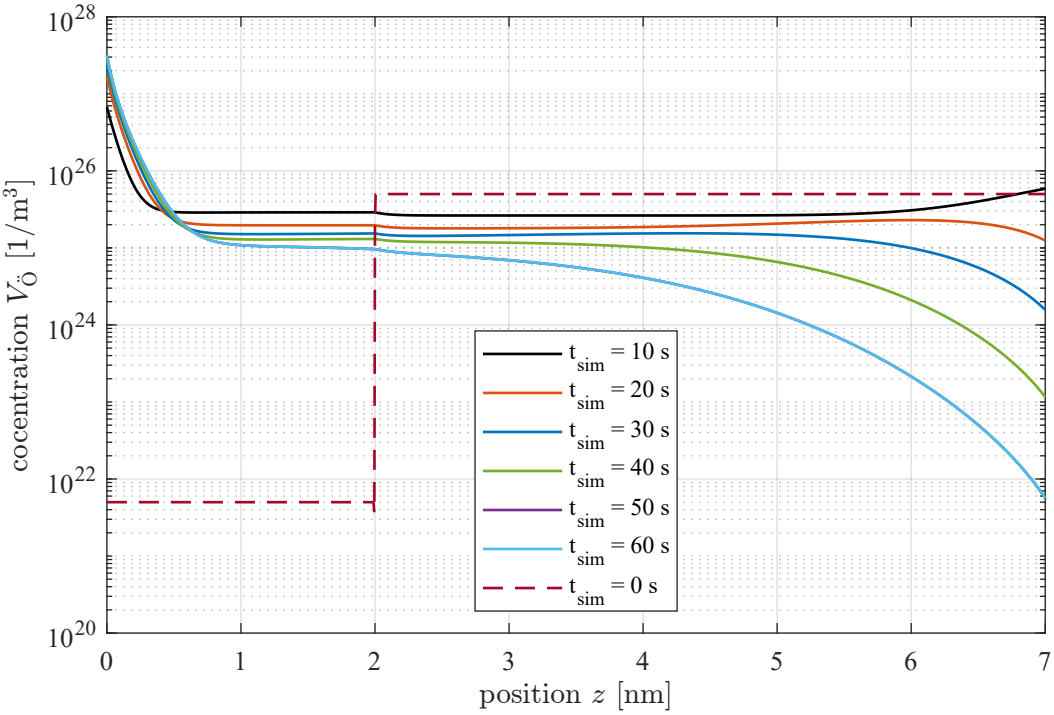

Figure 4.21: $V_{\ddot{O}}(z)$ - Distribution of oxygen vacancies across the VCM layers after no voltage is applied to the top electrode. For 0 s, 10 s, 20 s, 30 s, 40 s, 50 s and 60 s of simulation.

tribution caused by diffusion. However, higher positive voltages result in a decreased concentration in the oxide 1 regions. With greater bias magnitude, the decrement occurs more rapidly, and the distribution approaches the initial value (derived from doping value) sooner.

To unravel the behavior behind the initial gradual decrease followed by a subsequent rapid linear decrease in the oxygen vacancy distribution within oxide 1 when positive voltages are applied, an in-depth analysis of the simulation results at various points in the geometry and different time intervals is conducted. Figure 4.25 illustrates the oxygen vacancy distribution initiated from the steady state and subjected to a positive voltage. The figure indicates that over time, the peak in the oxygen vacancy concentration gradually shifts towards the bottom electrode. Specifically, around $t_{\text{sim}} = 6$ s, the peak reaches the interface between oxide 1 and oxide 2. This observation aligns with the findings from Figure 4.24, wherein the rapid reduction of the mean value of $V_{\ddot{O}}$ in oxide 1 begins approximately 6 s after the voltage is applied.

4.4.3 Resistance states

In the preceding subsection, various states arising from the application of positive bias are explored, each potentially exhibiting distinct electrical properties. Given the relevance of characterizing resistance states in ReRAM studies, the focus now shifts to examining the resistance per area in these different states.

Figure 4.26 illustrates the resistivity of the device in various states of the oxygen vacancy concentration, starting from the relaxed state and the subsequent application of a +2 V bias. This conductivity is depicted over time to capture the evolution of resistance under the influence of the applied voltage. As depicted in Figure 4.26, transitioning away from the relaxed state and driving the peak in the oxygen vacancy concentration distribution towards the bottom electrode initially leads to a significant

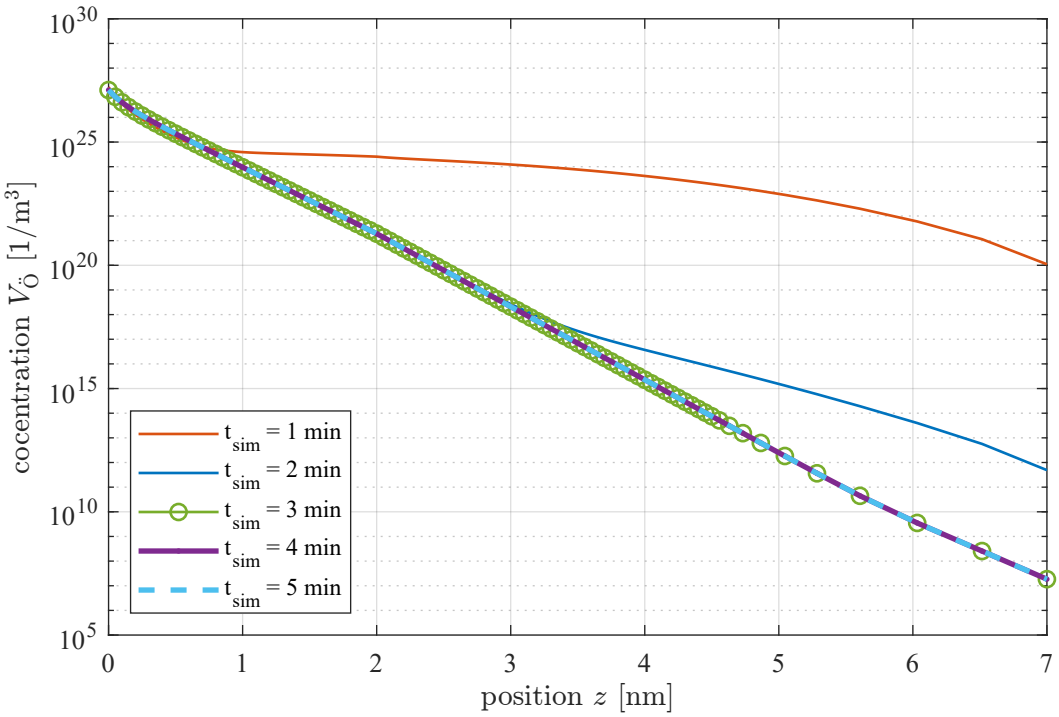

Figure 4.22: $V_{\ddot{O}}(z)$ - Distribution of oxygen vacancies across the VCM layers after no voltage is applied to the top electrode. For 1 min, 2 min, 3 min, 4 min, and 5 min of simulation. The result is stabilized after 3 minutes.

decrease in resistance. However, over time, this change becomes more gradual. This observation suggests that after a certain duration, most of the oxygen vacancies have migrated into the oxide 2 area, diminishing the time-dependent effect on resistance.

The findings obtained here are consistent with recent research conducted by Aussen et al. [27]. In their study, aimed at investigating the potentiation (enhancement of conductivity) of an Al_2O_3/TiO_x device, a sequence of short-term pulses (1 ms) was applied. Subsequently, the conductivity of the device was measured at each step. They observed a rise in conductivity with increasing duration of positive bias application. Similar to the results observed in this subsection, the change in conductivity exhibited a non-linear behavior, initially increasing rapidly before tending towards saturation. The same behavior was also observed during depression (lowering the conductivity with negative voltage).

To validate the observed phenomena in reverse, the oxygen vacancy distribution resulting from applying a +2 V bias for 30 s is preserved as the starting point (representing the LRS), initiating a new simulation. This simulation commences from the LRS distribution and applies a negative bias.

Figure 4.27 shows the resistivity of the VCM device and the mean oxygen vacancy concentration in oxide 1 at various time intervals, originating from the LRS distribution and subjected to a constant -2 V bias. It is evident from the figure that upon the application of a negative bias, the oxygen vacancies tend to migrate towards the oxide 1 regions, consequently leading to an increase in the device's resistance. Furthermore, the change in resistance is more pronounced at the outset, gradually attenuating as the oxygen vacancy concentration peak reaches the interface between the two oxide layers.

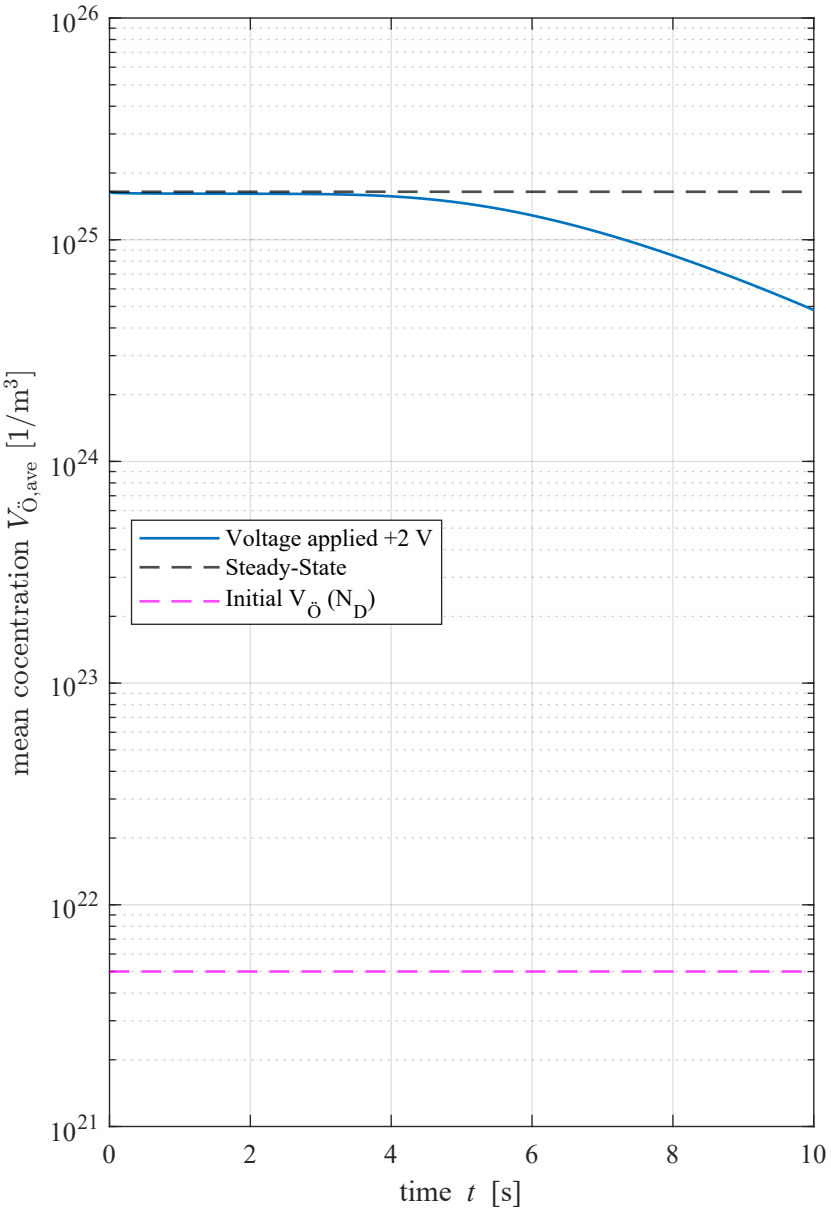

Figure 4.23: $V_{\ddot{O},ave}(t)$ - Mean value of the oxygen vacancy concentration in the oxide 1 region at different time intervals when a positive bias of +2 V is applied to the top electrode, with the initial distribution set to the relaxed state.

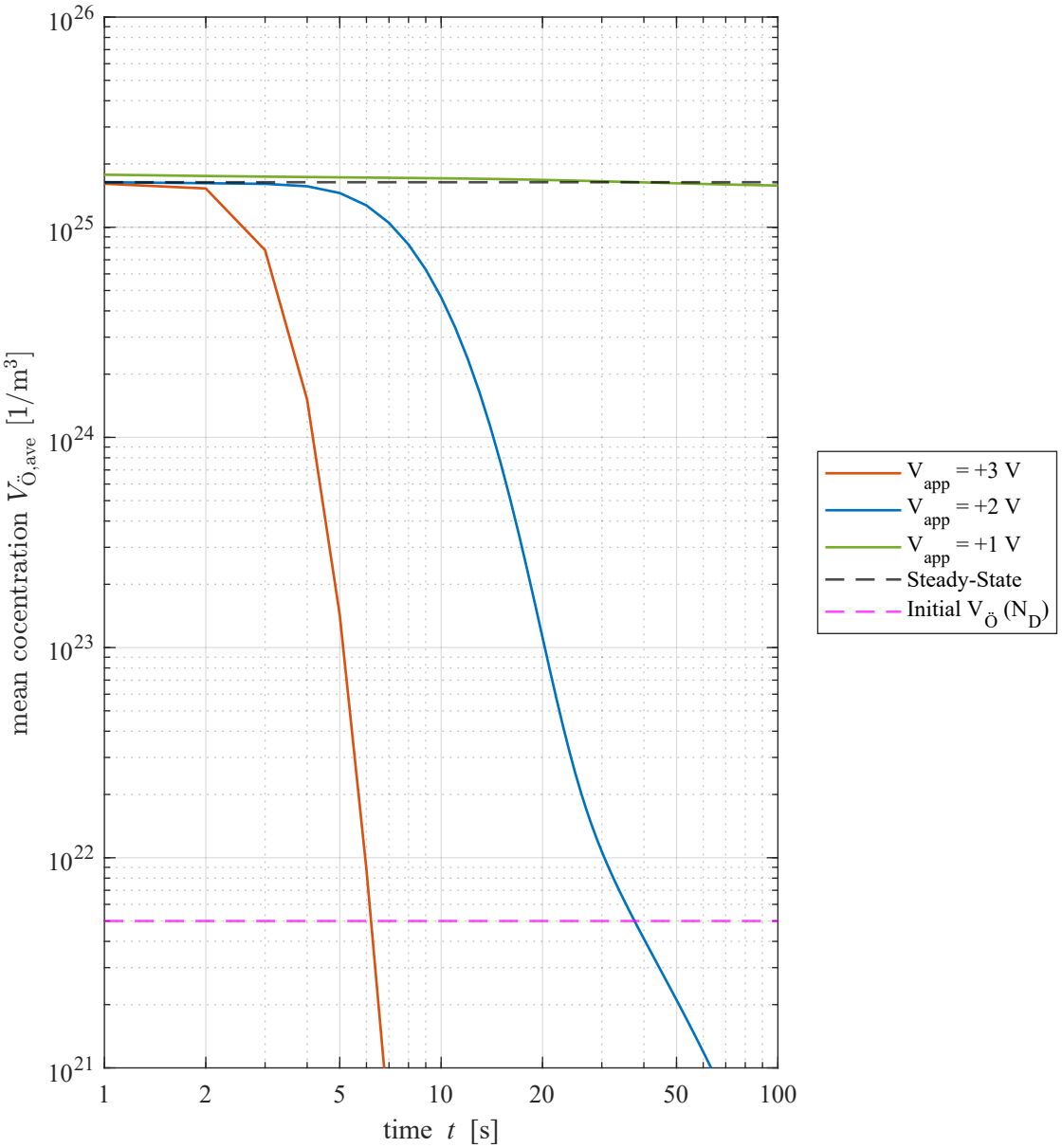

Figure 4.24: $V_{\ddot{O},ave}(t)$ - Mean value of the oxygen vacancy concentration in the oxide 1 region at different times, when voltages of +3 V (orange), +2 V (blue), and +1 V (green) are applied to the top electrode. The initial distribution corresponds to the relaxed state.

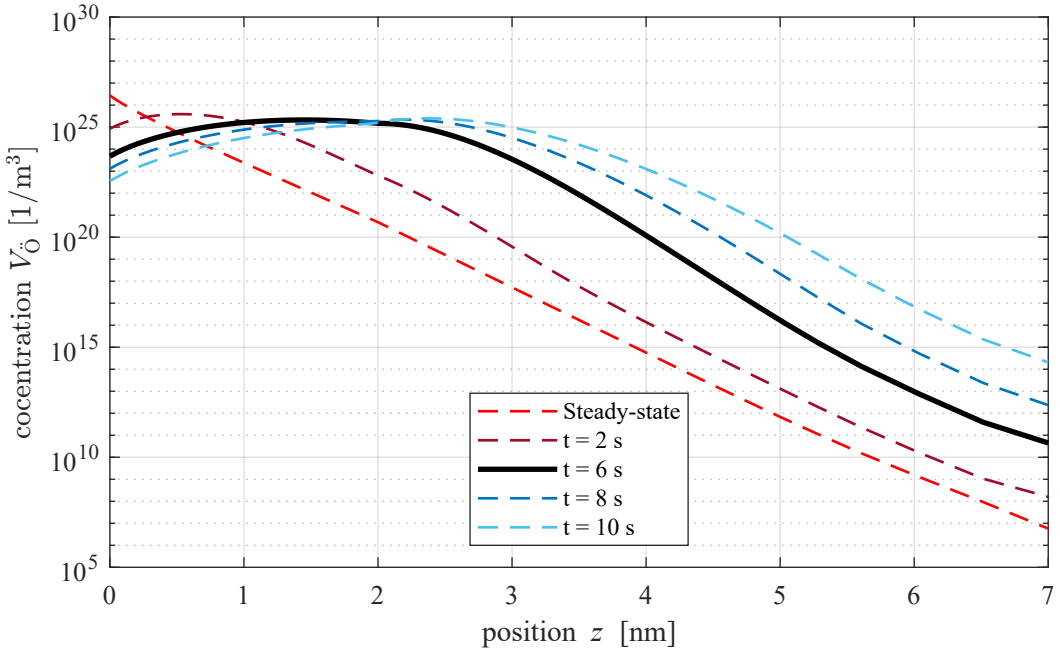

Figure 4.25: $V_{\ddot{O}}(z)$ - Oxygen vacancy concentration in different simulation domains when +2 V is applied to the top electrode. The red lines represent cases where the drop in the mean value of oxide 1 is minimal, the black line indicates the point where the maximum oxygen vacancy concentration is located near the interface, and blue lines correspond to cases where the decrement of the oxygen vacancy mean value is rapid for oxide 1 regions.

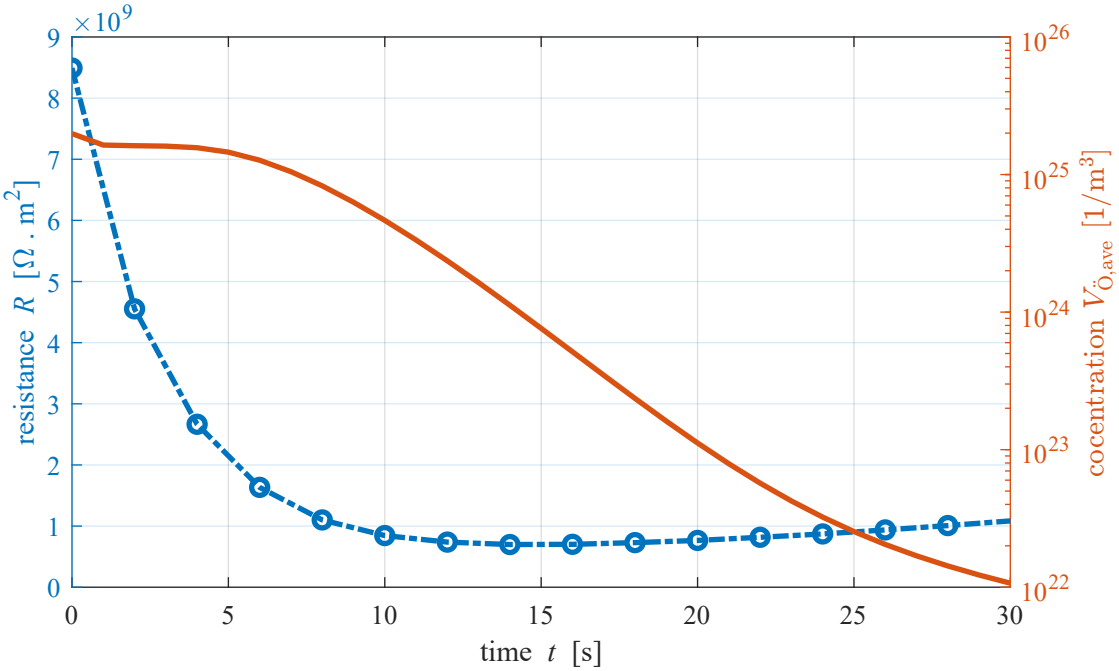

Figure 4.26: $R(t)$ vs. $V_{\ddot{O},ave}(t)$- Resistance times area measured for a +0.5 V bias in the middle of oxide 2 ($z = 4.5$ nm) versus the mean value of the doubly ionized oxygen vacancy concentration in oxide-1, in time evolution during which a +2 V bias is applied to the top electrode starting from the relax-state distribution.

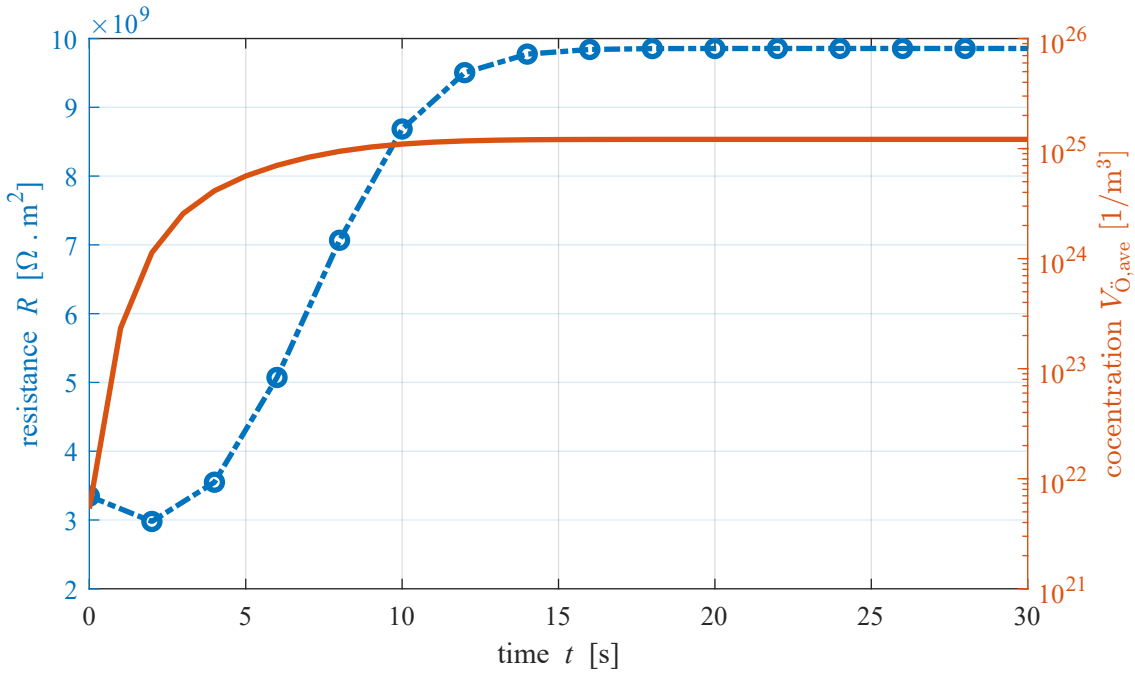

Figure 4.27: $R(t)$ vs. $V_{\ddot{\mathrm{O}},\mathrm{ave}}(t)$- Resistance times area measured for a +0.5 V bias in the middle of oxide 2 ($z = 4.5$ nm) versus the mean value of the doubly ionized oxygen vacancy concentration in oxide-1, in time evolution during which a -2 V bias is applied to the top electrode starting from the LRS distribution.

4.5 Phase II-a

In this phase of the simulation, the focus shifts to utilizing the COMSOL built-in Semiconductor Module. Here, the oxygen vacancy continuity equation, as described in Section 4.1, is implemented. Given the small fluctuations in temperature observed in previous phases (Appendix A), the heat conduction equation is disregarded. Instead of implementing the Poisson equation and electron continuity equation manually, the Semiconductor Module is employed, offering various methods for calculating and determining the required parameters. Detailed descriptions of the equations and methodologies can be found in [28]. The parameters used remain consistent with those outlined in Table 4.1. Due to issues arising from the initial values in the Semiconductor Module, leading to non-convergence during simulation, an additional step is introduced. This step involves conducting a semiconductor equilibrium study before initiating the time dependent study.
To compare the utilization of the built-in module with the self-implemented simulation, a pulsed voltage is once again applied to the top electrode of the VCM, akin to Sections 4.1 and 4.3. Figure 4.28 illustrates the behavior of the applied voltages in this phase, with pulse durations (simulation time) set at one and five seconds, and applied biases ranging from -2 V to $+2$ V.

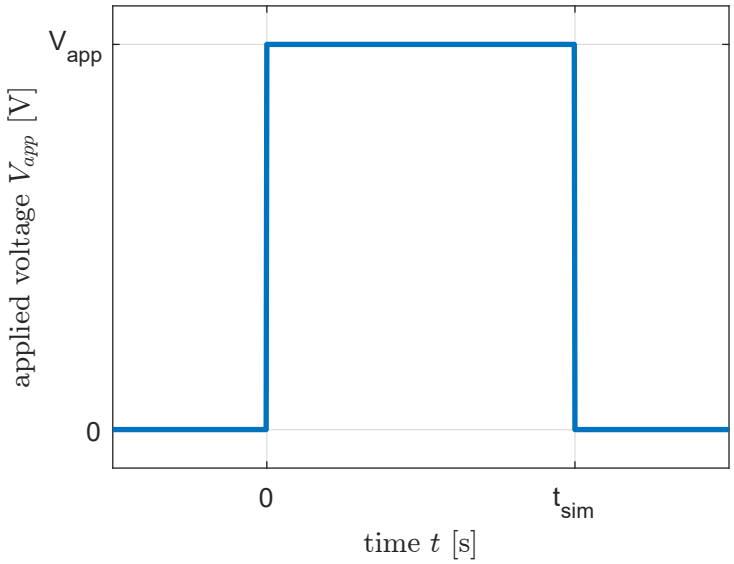

Figure 4.28: $V_{\mathrm{app}}(t)$ - Applied voltage function for simulation phase II-a. The increase and decrease of the voltage happens in a short time (10^{-5} s).

4.5.1 Effect of applied voltage

In the initial analysis, a comparison of results is conducted across different pulse durations. Oxygen vacancy concentration and conduction band energy following the application of voltage pulses to the top electrode are examined. The former is determined by solving the oxygen vacancy continuity equation, while the latter is obtained through the Semiconductor Module of the COMSOL software. Figure 4.29 illustrates the distribution of oxygen vacancies, while Figure 4.30 displays the conduction band energy level after pulses with duration of 1 s. Interestingly, unlike the self-implemented projects which were used in previous cases, the oxygen vacancy distribution ($V_{\dot{\mathrm{O}}}(z)$) and conduction band energy ($E_{\mathrm{C}}(z)$) remain consistent across different magnitudes and polarities of the applied pulse voltage when using the Semiconductor module of COMSOL Multiphysics software.

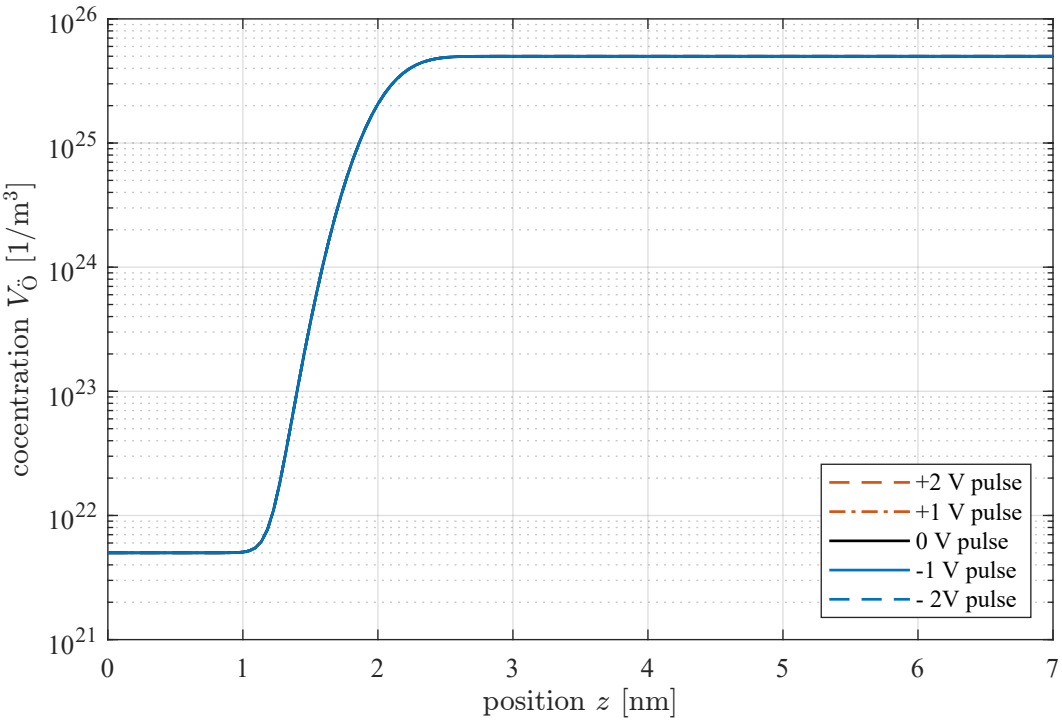

Figure 4.29: $V_{\ddot{O}}(z)$ - Oxygen vacancy distribution across different positions of the VCM structure under external voltage pulses applied for durations of one second. The black line represents the case without external voltage, while orange and blue lines depict positive and negative pulse voltages, respectively. Results are derived from solving the ion continuity equation and using the built-in Semiconductor module in COMSOL. Since all the lines have the same values everywhere, the orange and black lines are not visible.

After examining the results from one-second pulses, a similar approach is employed for a pulse duration of 5 s to corroborate the findings. Figure 4.31 demonstrates the distribution of oxygen vacancies, while Figure 4.32 shows the conduction band energy level following five-second duration pulses. Similar to the previous case, the oxygen vacancy distribution ($V_{\ddot{O}}(z)$) and conduction band energy ($E_C(z)$) exhibit consistency across various magnitudes and polarities of the applied pulse voltage when utilizing the Semiconductor Module of COMSOL Multiphysics software, contrasting with the results obtained from the self-implemented project.

Regarding the obtained results in this phase, the difference observed in the behavior when utilizing the built-in Semiconductor Module compared to the implementation of equations using simple mathematical modules in COMSOL Multiphysics is currently unclear. These unexpected differences raises questions regarding the underlying algorithms and numerical methods employed in the Semiconductor Module, as well as the accuracy of its simulations compared to custom implementations.

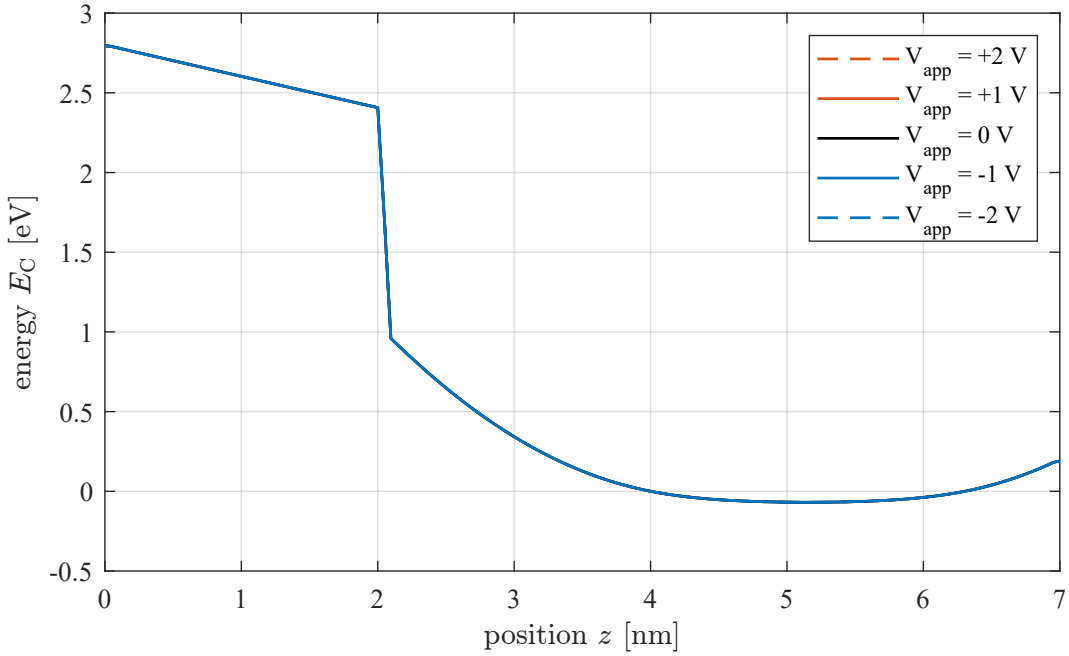

Figure 4.30: $E_C(z)$ - Conduction band energy across various positions of the VCM bi-layer structure after applying pulsed voltage for one second. The black line denotes the case without external voltage, while orange and blue lines represent positive and negative pulse voltages, respectively. Results are obtained from solving the ion continuity equation and employing the built-in Semiconductor Module in COMSOL. Since all the lines have the same values everywhere, the orange and black lines are not visible.

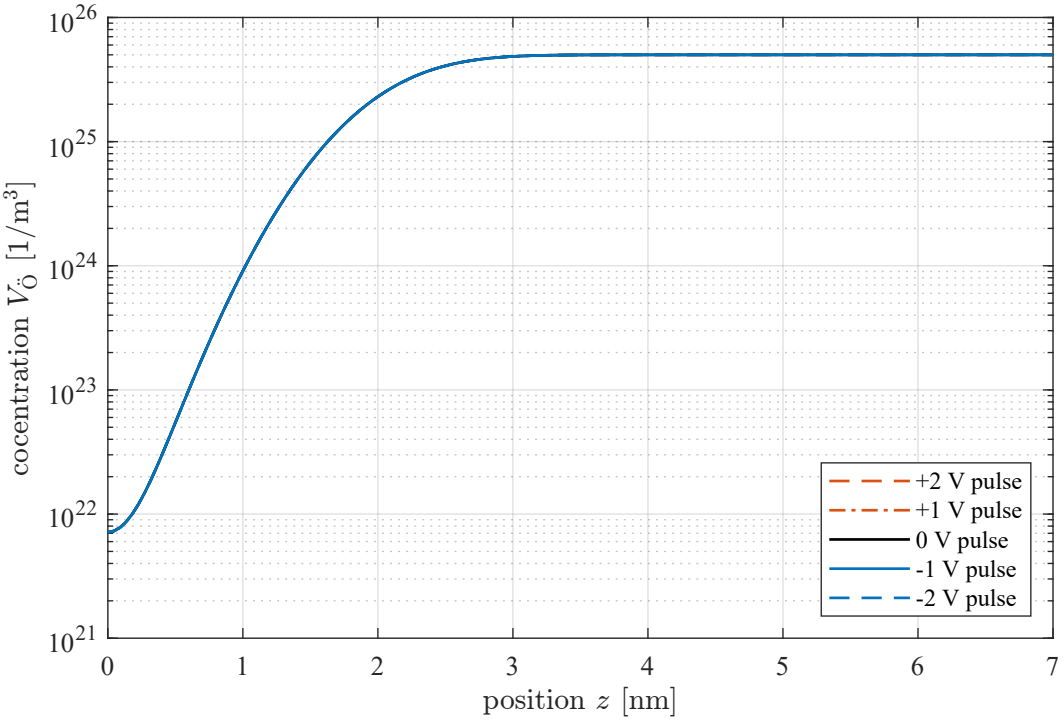

Figure 4.31: $V_{\ddot{O}}(z)$ - Oxygen vacancy distribution across different positions of the VCM structure under external voltage pulses applied for durations of five seconds. The black line represents the case without external voltage, while orange and blue lines depict positive and negative pulse voltages, respectively. Results are derived from solving the ion continuity equation and using the built-in Semiconductor module in COMSOL. Since all the lines have the same values everywhere, the orange and black lines are not visible.

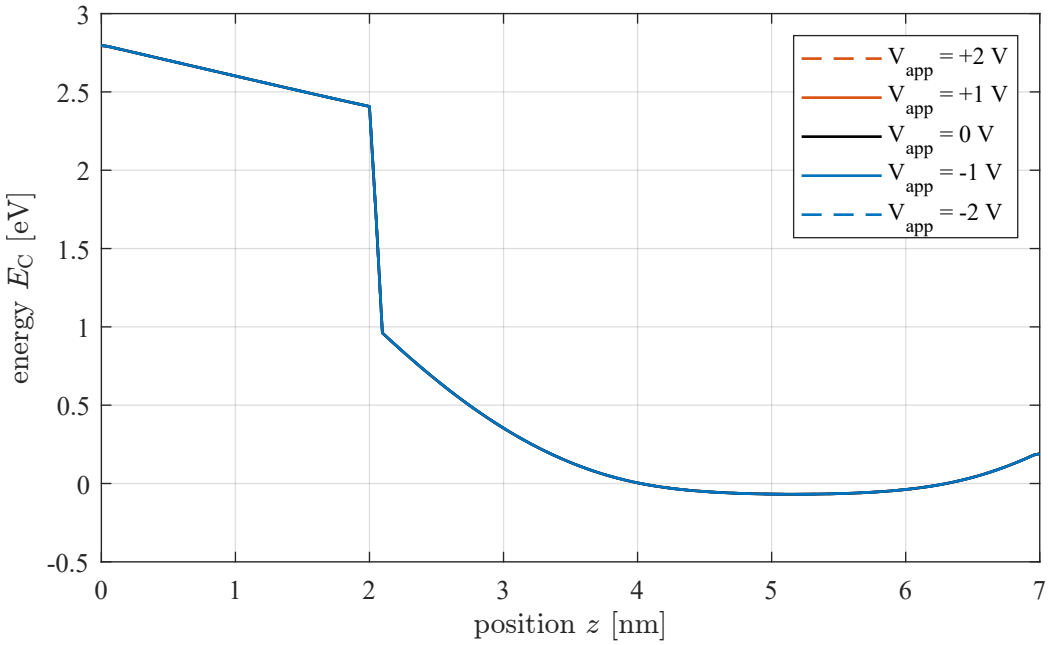

Figure 4.32: $E_C(z)$ - Conduction band energy across various positions of the VCM bi-layer structure after applying pulsed voltage for five seconds. The black line denotes the case without external voltage, while orange and blue lines represent positive and negative pulse voltages, respectively. Results are obtained from solving the ion continuity equation and employing the built-in Semiconductor Module in COMSOL. Since all the lines have the same values everywhere, the orange and black lines are not visible.

4.6 Phase II-b

After observing no significant change in the distribution of charge carriers following the coupling of the oxygen vacancy equation and Semiconductor Module in the previous phase of the simulation, it was decided to utilize the values obtained in phases I-a and I-c for $V_{\ddot{O}}(z)$ in Sections 4.1 and 4.3. subsequently, the oxygen vacancy equation was removed from the simulation, akin to Section 4.2. However, in this phase, the Semiconductor Module was employed to determine the JV-characteristics after applying a sweep voltage to the top electrode. Figure 4.33 illustrates the applied voltage to the VCM layers at different times during this phase of the simulation.

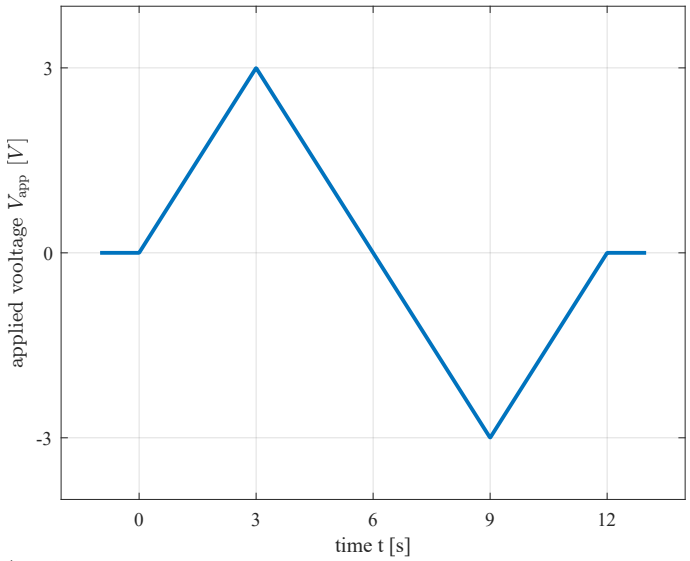

Figure 4.33: $V_{\text{app}}(t)$ - Applied voltage on the top electrode in the time evolution for phase II-b of the simulation.

4.6.1 Current-voltage characteristics

The critical variable to examine after subjecting the VCM model to sweep voltage simulation is the current density across different applied voltages, known as the JV characteristics. Although the Semiconductor Module computes various current densities, it is beneficial to focus on observing the drift electron current density along the z-axis, particularly at the midpoint of the second oxide layer. By analyzing these specific current results, one can compare them with the outcomes obtained in Section 4.2.

Despite numerous attempts, we were unable to successfully run the simulation using the built-in Module of the COMSOL software. The primary challenge arose from incorporating direct tunneling into the model, as convergence issues occurred consistently whenever attempts were made to include it. Even efforts to reconstruct the model based on a previously tested two-dimensional model for heterojunction tunneling [29] from the COMSOL website proved ineffective.

Furthermore, excluding direct tunneling from the model and applying sweep voltage to the top electrode did not yield the expected behavior in terms of current inside the device. Figure 4.34 illustrates an example of the current-voltage characteristics obtained from applying a sweep voltage to a device previously subjected to a 1 s pulse bias. As depicted in the plot, the changes in current throughout the voltage evolution do not align with expected outcomes.

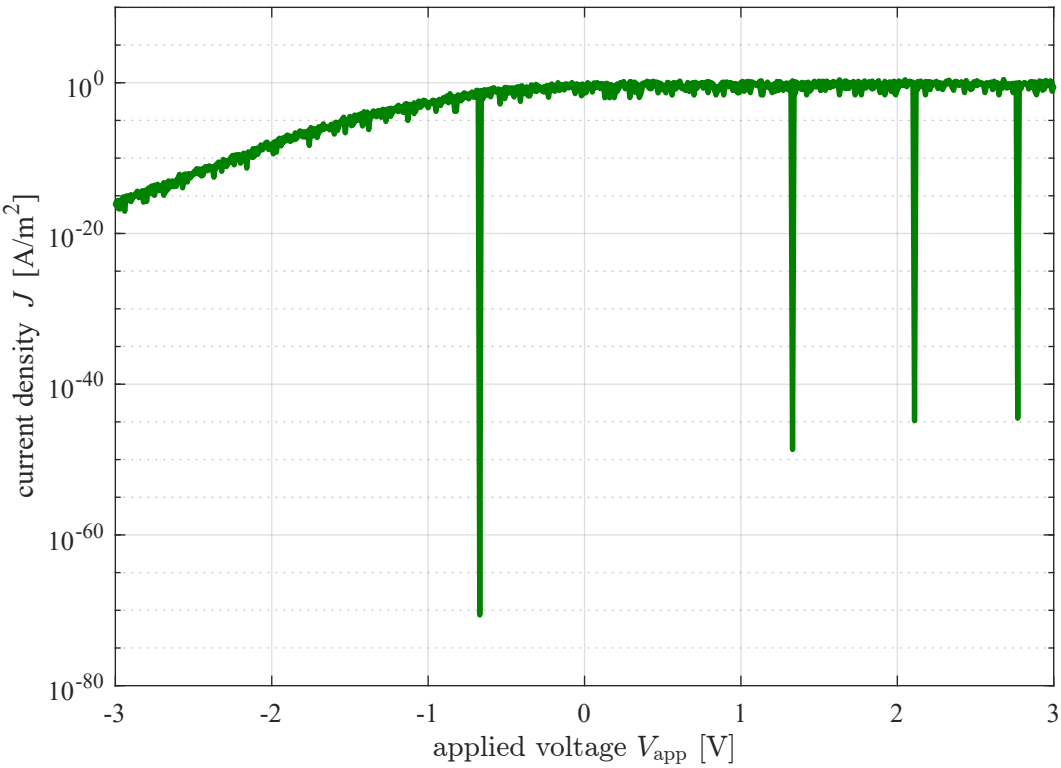

Figure 4.34: $J(V_{app})$ - Current density under different applied voltages, obtained using the Semiconductor Module, for a device previously subjected to a 1 s pulse with a bias of +1 V.

4.7 Phase III-a

In this simulation phase, the objective is to replicate the experiments conducted in Section 4.4, with the materials and geometry utilized by Aussen et al [27]. Consequently, while the methodologies and physical model remain consistent with the previously implemented projects, adjustments are made to the simulation parameters to align with the new materials (AlO_x and TiO_x), as detailed in Table 4.2.

4.7.1 Reaching relaxed state

The initial step involves seeking the relaxed-state (or steady-state) distribution of doubly ionized oxygen vacancies. This can be accomplished by removing the device from biasing and allowing the simulation to run for an extended duration until a stable distribution is attained.
Figure 4.35 illustrates the evolution of oxygen vacancy distribution across various sections of the VCM device over time. After five minutes of simulation, a noticeable change persists in the oxygen vacancy concentration, indicating the necessity for longer simulation durations to achieve a steady-state. Figure 4.36 illustrates the oxygen vacancy concentration distribution after allowing the device to remain unbiased for up to 20 minutes. As depicted in the plot, with increasing time, the doubly ionized vacancies tend to migrate from areas corresponding to the oxide 2 region towards regions near the top electrode (oxide 1 areas). After a period (around 12 min), the distribution stabilizes, reaching a steady-state where further increases in time do not significantly alter the vacancy concentration. This distribution can be regarded as the relaxed-state oxygen vacancy concentration for subsequent analyses.
Comparison with results obtained in Section 4.4 reveals a longer time required to reach the steady-

Parameter	Symbol	Value	Unit
oxide 1 thickness	t_{oxide1}	1.2	nm
oxide 2 thickness	t_{oxide2}	7	nm
electron affinity of oxide 1	χ_1	2.58	eV
electron affinity of oxide 2	χ_2	3.5	eV
relative permittivity of oxide 1	ϵ_{r1}	2.2	
relative permittivity of oxide 2	ϵ_{r2}	8	
thermal conductivity of oxide 1	κ_1	1	$\text{W}/(\text{m} \cdot K)$
thermal conductivity of oxide 2	κ_2	1	$\text{W}/(\text{m} \cdot K)$
electron mobility of oxide 1	μ_{n1}	5	$\text{cm}^2/(\text{V} \cdot \text{s})$
electron mobility of oxide 2	μ_{n2}	10	$\text{cm}^2/(\text{V} \cdot \text{s})$
effective electron mass for oxide 1	$m_{\text{eff,n1}}$	$0.25 \cdot m_{\text{e}}$	kg
effective electron mass for oxide 2	$m_{\text{eff,n2}}$	$0.25 \cdot m_{\text{e}}$	kg
initial density of donor dopants for oxide 1	N_{D1}	$1 \cdot 10^{16}$	$1/\text{cm}^3$
initial density of donor dopants for oxide 2	N_{D2}	$1 \cdot 10^{20}$	$1/\text{cm}^3$
diffusion coefficient pre-factor for oxide 1	D_{01}	$1 \cdot 10^{-7}$	cm^2/s
diffusion coefficient pre-factor for oxide 2	D_{02}	$1 \cdot 10^{-7}$	cm^2/s
oxygen ion activation energy for oxide 1	W_{A1}	0.5	eV
oxygen ion activation energy for oxide 2	W_{A2}	0.5	eV
top electrode metal work function (Pt)	$W_{\text{M,top}}$	5.84	eV
bottom electrode metal work function (Cr)	$W_{\text{M,bottom}}$	4.5	eV

Table 4.2: Parameters used in simulation from [27] (m_{e} denotes the electron mass).

state for the new device with the set parameters. this difference might be due to the fact that from the current device having a longer geometry, resulting in a lengthier diffusion process required for saturation.

4.7.2 Oxygen vacancy concentration and resistance state

After identifying the relaxed-state distribution of doubly ionized oxygen vacancies across the device, we attempted to apply positive and negative voltages to the device to observe changes in both oxygen vancancies and resistance of the VCM Bi-Layer structure. However, numerical errors (non convergings) prevented us from obtaining usable results. These failures could be due to the high levels of oxygen vacancy concentration near the top electrode, as shown in Figure 4.36. We could not find a solution to address this issue while trying to achieve the relaxed-state in Subsection 4.7.1.

4.7.3 Effect of electrode metal material

In this phase of the simulations, all parameters listed in Table 4.2 remained constant. The only alteration was the substitution of the material for the bottom electrode with Platinum, matching it with the top electrode. To implement this change, the metal work function of the bottom electrode was adjusted to 5.84 eV, aligning it with the top electrode.

The subsequent step involved letting the simulation run without applying any bias to the device while monitoring changes in oxygen vacancy concentration to establish a relaxed-state distribution. Figure 4.37 illustrates the oxygen vacancy concentration across different segments of the device under the absence of external bias. Over time, the vacancies tend to accumulate near the electrodes and move away from the oxide regions.

Comparing the recent findings with those outlined in Subsection 4.7.1 yields two conclusions. Firstly, employing two metals with identical work functions for the top and bottom electrodes leads to a

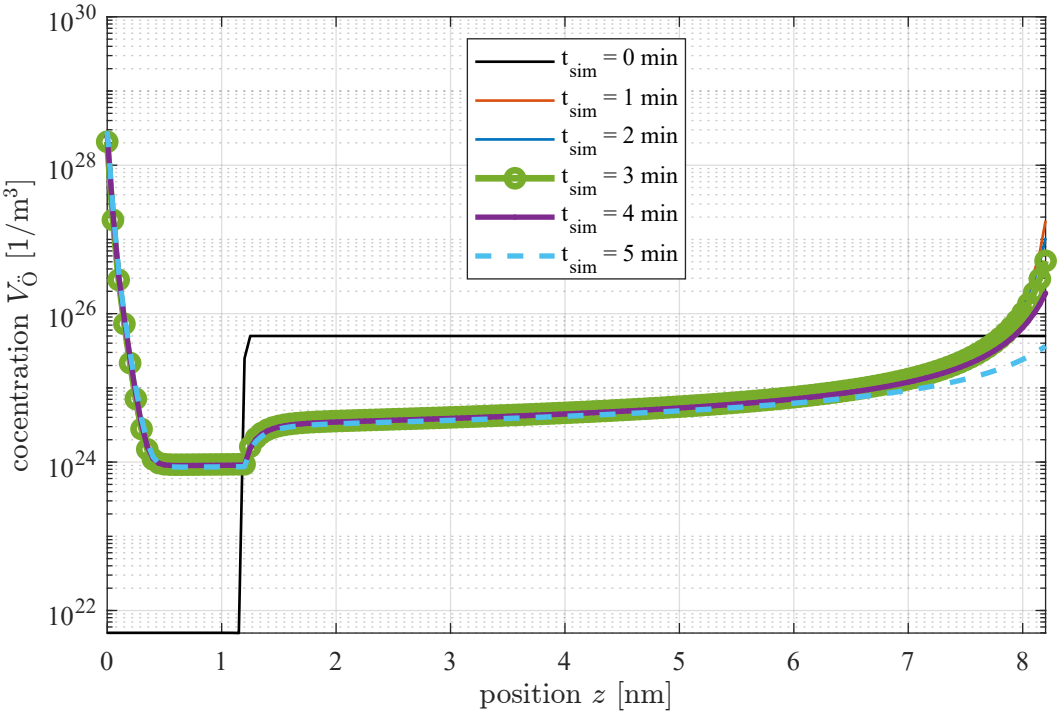

Figure 4.35: $V_{\ddot{O}}(z)$ - Distribution of oxygen vacancies across the VCM layers after no voltage is applied to the top electrode. For 0 min, 1 min, 2 min, 3 min, 4 min, and 5 min of simulation.

symmetric distribution of oxygen vacancies in the relaxed-state. This contrasts with the scenario where different materials are used, where vacancies tend to accumulate primarily around the electrode with the higher metal work function. Secondly, in the simulations conducted in this subsection, the relaxed-state is achieved more rapidly due to the reduced need for vacancy movement.

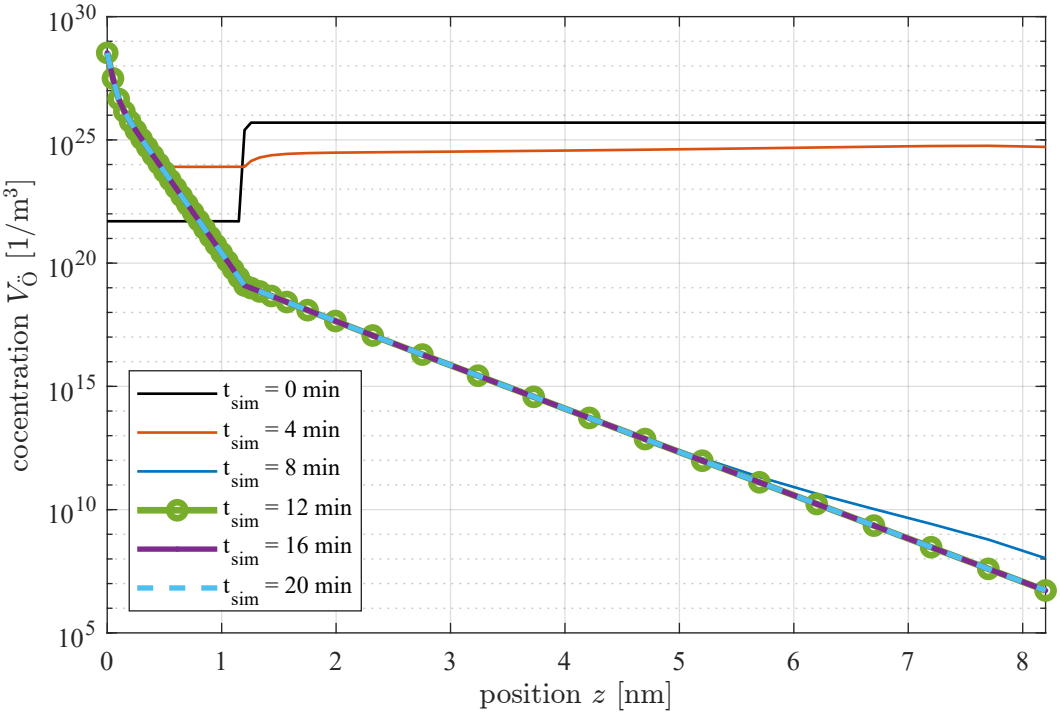

Figure 4.36: $V_{\ddot{O}}(z)$ - Distribution of oxygen vacancies across the VCM layers after no voltage is applied to the top electrode. For 0 min, 4 min, 8 min, 12 min, 16 min, and 20 min of simulation.

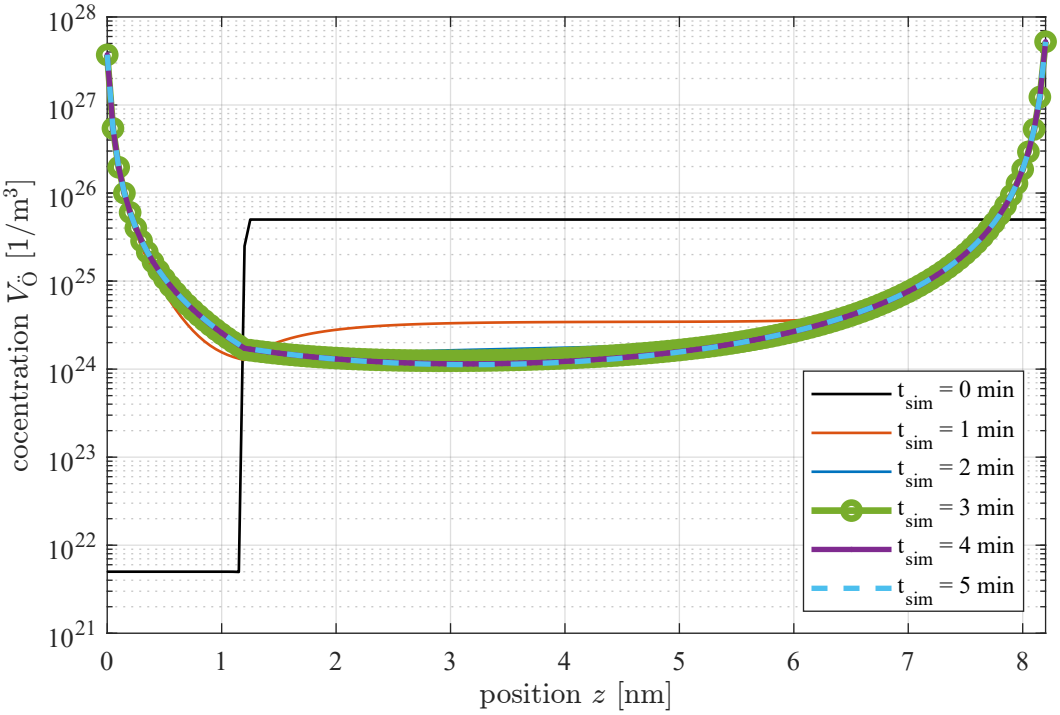

Figure 4.37: $V_{\ddot{O}}(z)$ - Distribution of oxygen vacancies across the VCM layers after no voltage is applied to the top electrode. For 0 min, 1 min, 2 min, 3 min, 4 min, and 5 min of simulation. When Platinum is used for bottom electrode material.

4.8 Discussion

The results obtained from simulating the VCM model with the implemented model demonstrate the expected changes in internal properties of the oxide layer upon the application of external voltages. Specifically, when external voltages are applied in the form of pulses, the alterations within the geometry are contingent upon the voltage magnitude, polarity, and duration of application. Of utmost importance among these changes is the variation in oxygen vacancy concentration. It is observed that positive voltages lead to a decrease in distribution within the oxide-1 regions, with a more pronounced effect as the voltage magnitude increases. Conversely, negatively biased pulses exhibit a reverse effect, increasing the concentration in oxide-1 areas, with the increment becoming more evident with larger negative voltages. Subsequently, an analysis of the current characteristics reveals that alterations in oxygen vacancy distribution can significantly impact the conductivity of the VCM cell. Configurations with higher oxygen vacancy distribution in oxide-1 regions exhibit greater electrical conductivity compared to those with lower vacancy levels, suggesting that changes in resistance state in a bi-layer VCM cell can be attributed to oxygen migration between the layers. Table 4.3 reports the behavior seen from applying 1 s pulses to the top electrode.

Table 4.3: Changes observed from applying 1 s pulses to the top electrode.

	with positive bias	**with negative bias**
$V_{\ddot{\mathrm{O}}}$ in oxide 1	lower	higher
$V_{\ddot{\mathrm{O}}}$ in oxide 2	higher	lower
E_{C} in oxide 1	no meaningful change	no meaningful change
E_{C} in oxide 2	no meaningful change	no meaningful change
J in positive V_{app}	lower	higher
J in negative V_{app}	lower	higher

Furthermore, the impact of pulse duration is investigated in the subsequent analysis. It is observed that as the simulation time increases, the dominance of oxygen vacancy diffusion becomes prevalent in most cases, resulting in an increase in $V_{\ddot{\mathrm{O}}}$ distribution within oxide-1 regions. This trend persists across different applied voltage values except for cases involving +2 V. Additionally, in longer pulse durations, a change in conduction band energy is observed, wherein positive pulses lead to a decrease in oxide-2 and negative pulses cause a rise in oxide-2 region, with the extent of change increasing with simulation duration, also in 0 V the conduction band energy increases in oxide 2 areas with increasing the duration. Table 4.4 reports the behavior seen from applying longer pulses to the top electrode. To delve deeper into oxygen vacancy behavior, the simulation time is extended to achieve the equilibrium distribution of vacancies, which is attained after three minutes. Subsequent simulations are then conducted with the oxygen vacancy concentration set to the equilibrium state at the outset, followed by the application of a positive voltage. Notably, applying a positive voltage to the top electrode results in a reduction in oxygen vacancies within oxide-1 regions, shifting them towards the second oxide. This effect is only feasible with positive voltages exceeding 2 V, with a faster decrease in the oxygen vacancy concentration occurring as the magnitude of the positive bias increases. Table 4.5 presents the duration required to attain the initial value of the oxygen vacancy distribution (doping) under the influence of a positive voltage applied to the top electrode, with the initial distribution set to the steady-state configuration.

To investigate the non-linear change observed in the mean value of oxygen vacancy concentration in oxide-1 over time, the evolution of the oxygen vacancy profile was examined at different time points starting from the relaxed state. It was observed that after the peak value of the $V_{\ddot{\mathrm{O}}}(z)$ distribution

Table 4.4: Changes observed in different parameters when the duration of applied pulse is increased, with respect to the cases with a pulse duration of 1 s.

	5 **s duration**	10 **s duration**
E_C in oxide 2 region	higher	higher
$V_{Ö}$ in oxide 1 in $V_{app} = 0$ V	higher	higher
$V_{Ö}$ in oxide 1 in $V_{app} < 0$ V	higher	higher
$V_{Ö}$ in oxide 1 in $V_{app} = +1$ V	higher	higher
$V_{Ö}$ in oxide 1 in $V_{app} = +2$ V	lower	lower

Table 4.5: Time taken to reach the initial $V_{Ö}$ mean value in oxide-1 for different positive voltages when the starting concentration is the steady-state distribution.

Applied voltage [V]	**Time to reach initial value [s]**
+1	did not reach after 100
+2	37
+3	6

reached the interface, the decrease in vacancy concentration mean value became more pronounced. Subsequently, the resistance state corresponding to each distribution of oxygen vacancy concentration after applying positive voltage to the steady-state device was measured. After the point at which the peak value of vacancies reached the oxide 1-oxide 2 interface, the decrease in resistance slowed down and tended to saturate. This suggests a relation between oxygen vacancy dynamics and electrical conductivity within the device. The complementary effect becomes apparent upon applying a negative bias to the top electrode, initiating from the previous low resistance distribution. This manifests as an increase in the oxygen vacancy concentration within the oxide-1 regions, alongside a rise in the device's resistance. Table 4.6 provides a summary of the properties associated with the various resistance states obtained from simulations conducted on the VCM bi-layer device.

Following the examination of pulse and steady applied biases using a simulation constructed with the outlined physical model, an attempt was made to replicate the experiment using a built-in module within the COMSOL Multiphysics software, namely the Semiconductor Module. However, unlike the findings in the preceding phases, the alteration in the internal properties of the VCM layers, such as oxygen vacancy concentration and conduction band energy, is not apparent after applying pulses with varying polarity and magnitude. These simulations only reveal the effect of pulse duration, with the reason for such behavior remaining unknown.

After exploring the effects of pulsed biases using the Semiconductor Module, attempts were made to determine the resistance of the device in various states based on the previous distribution of oxygen vacancies via applying sweep voltages. However, these attempts were unsuccessful as well.

In the final stages of the simulations, a different set of material parameters was tested using the same methods as before. These materials were sourced from a previous study, with the goal of examining how the distribution of oxygen vacancy concentration behaves under various biases. Once again, when the device was left unbiased for a period, a relaxed-state was observed in the vacancy concentration, with higher concentrations near the top electrode. The only notable difference was the longer time required to reach this state, likely due to the device's longer geometry with the new parameters. However, when the device was subjected to external bias, the simulations did not converge. As a diagnostic test, the material used for the bottom electrode was changed to observe its effect. The results revealed that the distribution of oxygen vacancies in the relaxed-state is influenced by the metal work functions of the device electrodes. Vacancies tend to migrate towards the electrode with the higher work function at equilibrium. Additionally, if the same material is used for both the top

Table 4.6: Resistance states in the VCM ReRAM model with corresponding applied biases, resistances, and vacancy concentrations in oxide-1. Obtained from simulations with parameters reported in Table 4.1.

Resistance State	**Applied Bias**	**Resistance** $[\Omega.m^2]$	**Vacancy Concentration in Oxide-1**
HRS (OFF)	Negative	$\approx 10 \times 10^9$	High
LRS (ON)	Positive	$\approx 1 \times 10^9$	Low

and bottom electrodes, the distribution of oxygen vacancies within the device becomes symmetric.

Chapter 5

Summary and outlook

5.1 Summary

This thesis focuses on 1-D simulations conducted on a ReRAM VCM bi-layer structure composed of Hafnium oxide and Tantalum oxide. These simulations were performed using the finite element method with COMSOL Multiphysics software. The thesis outlines the physical model and equations employed to construct the simulation, including boundary conditions and additional properties.
Two distinct approaches were utilized in the simulation process. Initially, the differential equations were directly implemented, followed by the utilization of existing built-in physical models within the software.
Across the implemented phases, the effects of applying pulsed voltages to the device were investigated. The results indicate that external bias application can induce changes in internal properties of the stacked layers, notably in the concentration of doubly ionized oxygen vacancies and conduction band energies. These alterations are dependent on the magnitude, polarity, and duration of the applied bias, with higher voltages and longer durations magnifying the effects. These changes in material properties can subsequently influence the conductivity of the device, which is a key feature of ReRAM technology.
To deepen our understanding of the relationship between oxygen exchange between the layers and the electrical resistance of the device, efforts were made to achieve a steady-state (relaxed-state) by applying zero voltage to the device for an extended period. Subsequently, starting from the relaxed state and applying positive bias, changes in oxygen vacancy concentration and, consequently, resistance were observed. The simulation was also done in reversed manner, applying negative voltage to the previously positive-biased device. A distinct relationship was observed between the vacancy concentration within the oxide 1 (conducting oxide) and the resistance state of the device. In essence, a higher concentration of oxygen vacancies within the oxide 1 region corresponds to a high resistance state, while a lower concentration in oxide 1 leads to a low resistance state. This temporal evolution

was evident in the time-dependent results, with initial rapid changes followed by saturation as most of the oxygen vacancies migrated toward bottom electrode (oxide 2 regions). In summary, applying a positive voltage of adequate magnitude can be likened to the SET process, while the application of a sufficiently negative bias initiates the RESET process. Both processes exhibit time dependence.
In contrast, while utilizing the built-in module, attempts to replicate the same pulse measurements did not yield anticipated results for unknown reasons. In a subsequent phase, efforts were made to measure the conductivity of the device using the distributions obtained from the implemented phases, again those simulation were not successful. The reasons behind the received errors are not clear.
In the final stages, we tested different material parameters and observed the behavior of oxygen vacancy concentration under various biases. Despite achieving a relaxed-state in vacancy concentration, convergence issues arose during simulations under external bias. We experimented with altering the material for the bottom electrode, revealing a dependency on metal work functions. This affected vacancy migration towards the electrode with the higher work function and led to symmetric vacancy distribution when using identical materials for both electrodes.

5.2 Outlook

Throughout this thesis, a limited set of parameters were investigated to understand their impact on the internal and external properties of the bi-layer VCM ReRAM device. However, due to challenges encountered in numerical modeling, further exploration with a more sophisticated physical model may be necessary to overcome these simulation difficulties. This advanced model could facilitate the testing of a wider range of materials and geometries, providing deeper insights into device behavior.
Moreover, the use of the built-in Semiconductor Module within the COMSOL Multiphysics software did not prove effective for analyzing a 1-D model when ion charge carriers were included, and attempts to implement direct tunneling were unsuccessful. Therefore, it is recommended that an improved module be developed to address these issues and enhance the analysis capabilities for such devices.

Appendix A

Temperature fluctuation results

Figure A.1 illustrates the temperature variations across the VCM layer at different time intervals during phase I-a simulation with $V_{\text{app}} = 2$ V. It is evident from the plot that the temperature changes are negligible, indicating their insignificance in the simulation results.

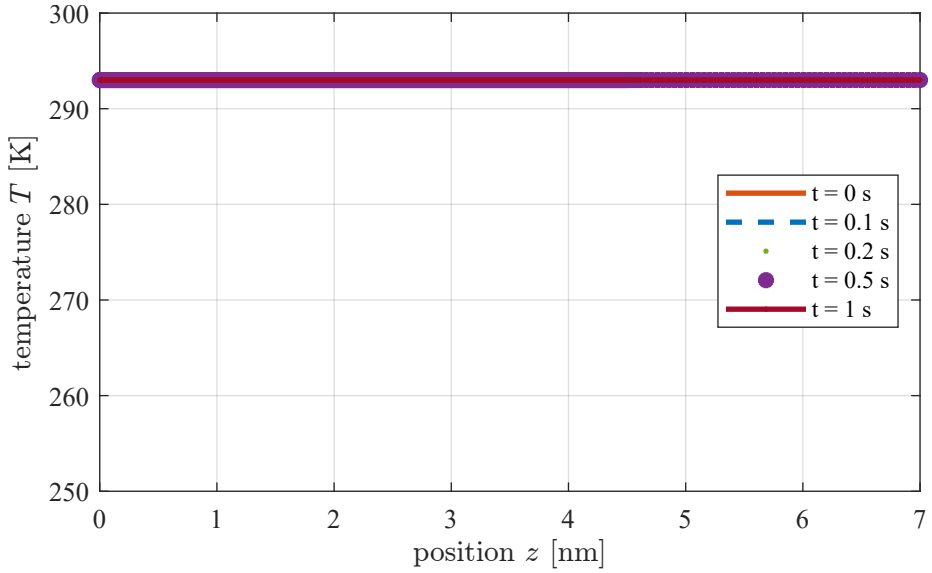

Figure A.1: $T(z)$ - Temperature in different parts of the VCM layers in different times of the simulation when +2 V pulse is applied to the top electrode for one second.

List of Figures

List of Tables

Bibliography

[1] Rainer Waser, Regina Dittmann, Georgi Staikov, and Kristof Szot. Redox-Based Resistive Switching Memories – Nanoionic Mechanisms, Prospects, and Challenges. *Advanced Materials*, 21(25-26):2632–2663, 2009.

[2] J. Joshua Yang, Dmitri B. Strukov, and Duncan R. Stewart. Memristive devices for computing. *Nature Nanotechnology*, 8(1):13–24, 2012.

[3] L. Chua. Memristor-The missing circuit element. *IEEE Transactions on Circuit Theory*, 18(5):507–519, 1971.

[4] Leon Chua. *Resistance Switching Memories Are Memristors*, pages 21–51. Springer International Publishing, 2014.

[5] A. V. Fadeev and K. V. Rudenko. To the Issue of the Memristor's HRS and LRS States Degradation and Data Retention Time. *Russian Microelectron*, 50(5):311–325, 2021.

[6] Matthias Wuttig and Noboru Yamada. Phase-change materials for rewriteable data storage. *Nature Material*, 6(11):824–832, 2007.

[7] Michael N. Kozicki, Maria Mitkova, and Ilia Valov. Electrochemical Metallization Memories. In *Resistive Switching*, pages 483–514. John Wiley Sons, Ltd, 2016.

[8] M. N. Kozicki, M. Yun, L. Hilt, and A. Singh. Applications of programmable resistance changes in metal-doped chalcogenides. In *Electrochemical Society, MEETING ABSTRACTS- ELECTROCHEMICAL SOCIETY -ALL DIVISIONS-*, number 1, page 849. Electrochemical Society;, 1999.

[9] Stephan Menzel, Matthias Waters, Astrid Marchewka, Ulrich Böttger, Regina Dittmann, and Rainer Waser. Origin of the Ultra-nonlinear Switching Kinetics in Oxide-Based Resistive Switches. *Advanced Functional Materials*, 21(23):4487–4492, 2011.

[10] Chun-Yang Huang, Chung-Yu Huang, Tsung-Ling Tsai, Chun-An Lin, and Tseung-Yuen Tseng. Switching mechanism of double forming process phenomenon in ZrOx/HfOy bilayer resistive

switching memory structure with large endurance. *Applied Physics Letters*, 104(6):062901, 02 2014.

[11] Fenja Berg. Simulation, fabrication and electrical characterisation of ReRAM bilayer structures: Understanding the influence of stacked oxides on forming and switching behaviour of ReRAM. Master's thesis, RWTH Aachen, 2017.

[12] Astrid Marchewka. *A numerical simulation model of valence-change-based resistive switching.* PhD thesis, RWTH Aachen, 2017.

[13] R. Waser. *Nanoelectronics and Information Technology.* Wiley-VCH, 2012.

[14] Benedikt Arndt, Francesco Borgatti, Francesco Offi, Monifa Phillips, Pedro Parreira, Thorsten Meiners, Stephan Menzel, Katharina Skaja, Giancarlo Panaccione, Donald A. MacLaren, Rainer Waser, and Regina Dittmann. Spectroscopic indications of tunnel barrier charging as the switching mechanism in memristive devices. *Advanced Functional Materials*, 27(45):1702282, 2017.

[15] Lesly E. Smart and Eliane A. Moore. *Solid State Chemistry: An Introduction.* Taylor & Francis, 1995.

[16] S.M. Sze and Kwok K. Ng. Metal-Semiconductor Contacts. In *Physics of Semiconductor Devices*, pages 134–196. John Wiley Sons, Ltd, 2006.

[17] Stefano Larentis, Federico Nardi, Simone Balatti, David C. Gilmer, and Daniele Ielmini. Resistive Switching by Voltage-Driven Ion Migration in Bipolar RRAM—Part II: Modeling. *IEEE Transactions on Electron Devices*, 59(9):2468–2475, 2012.

[18] R. Tsu and L. Esaki. Tunneling in a finite superlattice. *Applied Physics Letters*, 22(11):562–564, 06 1973.

[19] Mario Lanza. A Review on Resistive Switching in High-k Dielectrics: A Nanoscale Point of View Using Conductive Atomic Force Microscope. *Materials*, 7:2155–2182, 2014.

[20] F. Nardi, S. Balatti, S. Larentis, and D. Ielmini. Complementary switching in metal oxides: Toward diode-less crossbar RRAMs. In *2011 International Electron Devices Meeting*, pages 31.1.1–31.1.4, 2011.

[21] Myoung-Jae Lee, Chang Bum Lee, Dongsoo Lee, Seung Ryul Lee, Man Chang, Ji Hyun Hur, Young-Bae Kim, Chang-Jung Kim, David H. Seo, Sunae Seo, U-In Chung, In-Kyeong Yoo, and Kinam Kim. A fast, high-endurance and scalable non-volatile memory device made from asymmetric Ta2O5x/TaO2x bilayer structures. *Nature Materials*, 10(8):625–630, 2011.

[22] Umesh Chand, Chun-Yang Huang, and Tseung Yuen Tseng. Mechanism of High Temperature Retention Property (up to 200 °C) in ZrO2-Based Memory Device With Inserting a ZnO Thin Layer. *IEEE Electron Device Letters*, 35:1019–1021, 2014.

[23] Zhongrui Wang, HongYu Yu, Xuan Anh Tran, Zheng Fang, Jinghao Wang, and Haibin Su. Transport properties of HfO_{2-x} based resistive-switching memories. *Phys. Rev. B*, 85:195322, May 2012.

[24] Bo Xiao and Satoshi Watanabe. Oxygen vacancy effects on an amorphous-TaOx-based resistance switch: a first principles study. *Nanoscale*, 6(17):10169–10178, 2014.

[25] COMSOL AB, Stockholm, Sweden. Comsol multiphysics® v.6.1. *https://www.comsol.com*, 2024.

[26] A. Gehring. *Simulation of Tunneling in Semiconductor Devices*. PhD thesis, Technische Universität Wien, 2003.

[27] Stephan Aussen, Felix Cüppers, Carsten Funck, Janghyun Jo, Stephan Werner, Christoph Pratsch, Stephan Menzel, Regina Dittmann, Rafal Dunin-Borkowski, Rainer Waser, and Susanne Hoffmann-Eifert. Correlation between Electronic Structure, Microstructure, and Switching Mode in Valence Change Mechanism Al2O3/TiOx-Based Memristive Devices. *Advanced Electronic Materials*, 9(12):2300520, 2023.

[28] COMSOL AB, Stockholm, Sweden. Semiconductor module user's guide. *COMSOL Multiphysics® v.6.1*, 2023.

[29] COMSOL. Heterojunction tunneling. `https://www.comsol.com/model/heterojunction-tunneling-65761`, 2023. Accessed on March, 2024.